RESEARCH ARTICLE

NANO · MICRO small
www.small-journal.com

Dynamically Reconstructed Fe-CoOOH Semi-Crystalline Electrocatalyst for Efficient Oxygen Evolution Reaction

Abdul Qayum, Karim Harrath, Rui Li, Abebe Reda Woldu, Paul K. Chu, Liangsheng Hu, Fushen Lu,* and Xiangdong Yao*

The development of robust and efficient electrocatalysts for the oxygen evolution reaction (OER) has been the main focus of water electrolysis but remains a great challenge. Here, the synthesis of a highly active and ultra-stable Fe-CoOOH electrocatalyst is reported by steering raw cobalt foam via an in situ solution combustion method assisted by a galvanic replacement reaction and subsequent electrochemical reconstruction of the $CoFeO_x$ pre-catalyst. *In/*ex situ electrochemical analysis and physicochemical characterizations show that the $CoFeO_x$ undergoes quick chemical and slow morphological reconstruction to Fe-CoOOH nanosheets. The Fe-CoOOH possesses a semi-crystalline nature with distinct short-range ordering and outstanding OER activity with overpotentials as low as 271 and 291 mV at current densities of 500 and 1,000 mA cm^{-2}, respectively. The remarkable stability under 1,000 mA cm^{-2} for at least 700 h is achieved. Theoretical calculations confirm the crucial role of Fe doping in facilitating surface reconstruction, enhancing OER activity, and improving the stability of the Fe-CoOOH. Comparative analysis with other transition metals doping reveals the unique ability of Fe to adsorb onto the CoOOH surface, thereby modulating the electronic density and facilitating faster adsorption of reaction intermediates. This work represents valuable insights into the surface reconstruction and doping processes.

1. Introduction

Renewable energy sources and green fuels are required to mitigate the effects of environmental pollution, global warming, and energy insecurity.[1] One of the best candidates with the potential to be a future energy carrier is hydrogen.[2] The most practical and green method for producing hydrogen fuel is water electrolysis,[3] as the required electricity can be harnessed from green renewable energy sources.[4] Hydrogen generation from water electrolysis consists of two reactions: the oxygen evolution reaction (OER) and the hydrogen evolution reaction (HER).[5] OER is more challenging and needs a large overpotential to break the strong O–O double bond, which is the rate-determining step in water electrolysis. Hence, significant attention has been dedicated to developing efficient electrocatalysts to minimize the overpotential and improve the stability of OER by using transition metal-based oxides, hydroxides, sulfides, phosphides, nitrides, and alloy-based catalysts.[6] In the meantime, some of these electrocatalysts have surpassed the performance of commercially available RuO_2 and IrO_2 catalysts[7]

Co-based catalysts have several advantages for the electrolysis of water due to their high OER activity, low cost, and mixed oxidation state, thus enabling the generation of various Co-based materials, including oxyhydroxides, hydroxides, sulfides, phosphides, oxides, and perovskite.[8] Several studies have reported that the initial state (pre-catalyst) of the electrocatalysts

A. Qayum, R. Li, A. R. Woldu, L. Hu, F. Lu
Department of Chemistry and Key Laboratory for Preparation and Application of Ordered Structural Materials of Guangdong Province
Shantou University
Shantou, Guangdong 515063, P. R. China
E-mail: lshu@stu.edu.cn; fslu@stu.edu.cn

K. Harrath
Fundamental Science Center of Rare Earths
Ganjiang Innovation Academy
Chinese Academy of Science
Guanzhou 341000, P. R. China

P. K. Chu
Department of Physics
Department of Materials Science and Engineering
and Department of Biomedical Engineering
City University of Hong Kong
Kowloon, Hong Kong, P. R. China

L. Hu, F. Lu, X. Yao
Chemistry and Chemical Engineering Guangdong Laboratory
Shantou 515063, P. R. China

X. Yao
School of Advanced Energy
Sun Yat-sen University (Shenzhen)
Shenzhen 518107, P. R. China

The ORCID identification number(s) for the author(s) of this article can be found under https://doi.org/10.1002/smll.202408854

DOI: 10.1002/smll.202408854

undergoes reconstruction under OER conditions, which greatly influences the OER activity as the performance of the catalyst is mainly dependent on the reconstructed phase and not on the initial state.[8f,9] The surface reconstruction of Co-based catalysts to CoOOH or $Co(OH)_2$, which are OER active electrocatalysts is beneficial, but their intrinsic low activity and poor stability stifle their applications in water electrolysis.[8c,f,10] Introduction of iron to Co or Ni hydroxide/oxyhydroxide electrocatalysts has several beneficial effects (Fe effects), including optimizing the binding energy of OER reaction, high conductivity, easing the reconstruction process, maintaining the intermediate spin state, dynamic active site generation and enduring excellent stability.[11] Another effective strategy to circumvent the sluggish OER kinetics is the creation of atomic defects and short-range ordering through the amorphization process.[12] Due to chemical homogeneity, atomic-scale structural flexibility, and an abundance of defects, semi-crystalline catalysts possess unique characteristics compared with pure crystalline materials. Although the aforementioned strategies are effective, few studies have explored the economic ramifications and commercial potential since these electrocatalysts with significant water-splitting activities and stability are primarily fabricated by complex and costly procedures. From a commercial point of view, the method to engineer OER electrodes must be facile, cost-effective, time-saving, and highly active, and the synthesized electrodes must be ultra-stable under large current density OER operations.[13]

Herein, we report a cost-effective, simple, and scalable in situ solution combustion-based method to rapidly steer raw Co foam (CF) into an ultra-stable, self-standing, and highly active Fe-doped CoOOH (Fe-CoOOH/CF) electrocatalyst for large current water oxidation with extra-long stability. The solution combustion synthesis method is a simple and efficient method to synthesize various types of nanomaterials and fabricate thin film electrodes in situ on substrates for different applications.[14] The as-constructed Fe-CoOOH/CF electrocatalyst shows excellent activities in OER and as an anode in two-electrode water-splitting systems in alkaline and alkaline seawater electrolysis with ultra-long stability. Combining the experimental results with density-functional theory (DFT) calculation, we unveil the unique adsorption behavior of Fe in comparison to other transition metals (Ni, Cu), which facilitates the reconstruction process and regulates the electronic density of the CoOOH catalyst to optimize the adsorption energy of oxygen intermediates thereby promoting the OER activity and stability. The performance is on par with or superior to the benchmark high current density (j_{HCD}) reported to date. This study demonstrates a major step toward the realization of commercial-level water electrolysis and hydrogen production and presents a novel way to design efficient electrocatalysts for electrochemical applications.

2. Results and Discussion

An in situ solution combustion method combined with an electrochemical surface reconstruction strategy is adopted to fabricate the Fe-CoOOH/CF electrocatalyst (**Figure 1a**). First, the $CoFeO_x$ pre-catalyst nanoparticles are grown on raw CF by the in situ solution combustion method. To initiate the combustion reaction, an oxidizer-fuel ($Fe(NO_3)_3$-ethylene glycol, EG) precursor solution is drop-casted on CF and preheated to 180 °C. Rapid combustion of the precursor solution takes place to steer the CF into porous $CoFeO_x$ nanoparticles (pre-catalyst) (Figure 1b; Figure S1, Supporting Information). No additional precursor is used for cobalt, but the CF substrate itself acts as a template to grow the $CoFeO_x$ nanoparticles. During the synthesis, the galvanic replacement reaction causes the outer surface of the CF to dissolve in the combustion solution, mix with Fe, and then redeposit as a result of the combustion reaction to yield $CoFeO_x$ nanoparticles. The galvanic replacement reaction is an effective approach to engineer various metal-based catalysts.[15] As the galvanic replacement reaction and combustion process take place on the surface of CF, the inner part of the CF remains intact thus maintaining good mechanical strength and firm connections between the $CoFeO_x$ pre-catalyst and CF substrate. Sudden evaporation of the solvent (fuel) generates a highly porous structure which is beneficial for the gas release during OER. Thermogravimetry-mass spectrometry (TG-DSC) is carried out to confirm the exothermic process and combustion reaction. The weight loss and heat release match well (Figure S2, Supporting Information).

The transformation of the $CoFeO_x$/CF pre-catalyst to Fe-CoOOH/CF can be achieved in situ through an electrochemical reconstruction process carried out under OER conditions. The electrochemical reconstruction process can be achieved by both chronopotentiometry (CP) and cyclic voltammetry (CV). Here, we include the results of the CP test (j = 1 A cm^{-2}, 48 h) as it is more realistic in practical applications. The CP and CV tests and their effects on the morphology and OER activities are described in the next section. The morphology of the as-reconstructed Fe-CoOOH/CF is examined by scanning electron microscopy (SEM), which shows that the $CoFeO_x$/CF pre-catalyst undergoes electrochemical reconstruction. After 48-h operation, the surface is completely converted to thin nanosheets uniformly grown on the surface (Figure 1c). XRD pattern shows no obvious peaks for the pre-catalyst and Fe-CoOOH/CF samples suggesting the existence of amorphous characters (Figure S1, Supporting Information). The surface reconstruction of the $CoFeO_x$/CF pre-catalyst is validated by transmission electron microscopy (TEM), which demonstrates that thin nanosheets are produced on the surface under OER conditions, consistent with the SEM images (Figure 1d). Interestingly, the reconstructed samples exhibit short-range ordering, which is characteristic of semi-crystalline materials, endowing them with superior catalytic application compared to their crystalline counterparts. According to the HR-TEM image, the apparent short-range order crystalline phases in the thin nanosheets arise from CoOOH (PDF # 26–0480), whereas the colored regions show the existence of amorphous character (Figure 1e). The selected-area electron diffraction (SAED) pattern of the Fe-CoOOH/CF sample exhibits several diffraction rings, revealing the presence of multiple phases and a semi-crystallized character, whereas the existence of a large halo confirms the semi-crystalline nature of the sample (Figure 1f). Combining the TEM with the XRD pattern further indicates that the catalyst mostly consists of amorphous components, hence no obvious XRD peaks can be observed for the Fe-CoOOH sample. The TEM-EDS elemental mapping and high-angle annular dark-field (HAADF) TEM image of the Fe-CoOOH/CF reveal the homogeneous distribution of Co, Fe, and O in the nanosheets, confirming doping of the Fe in

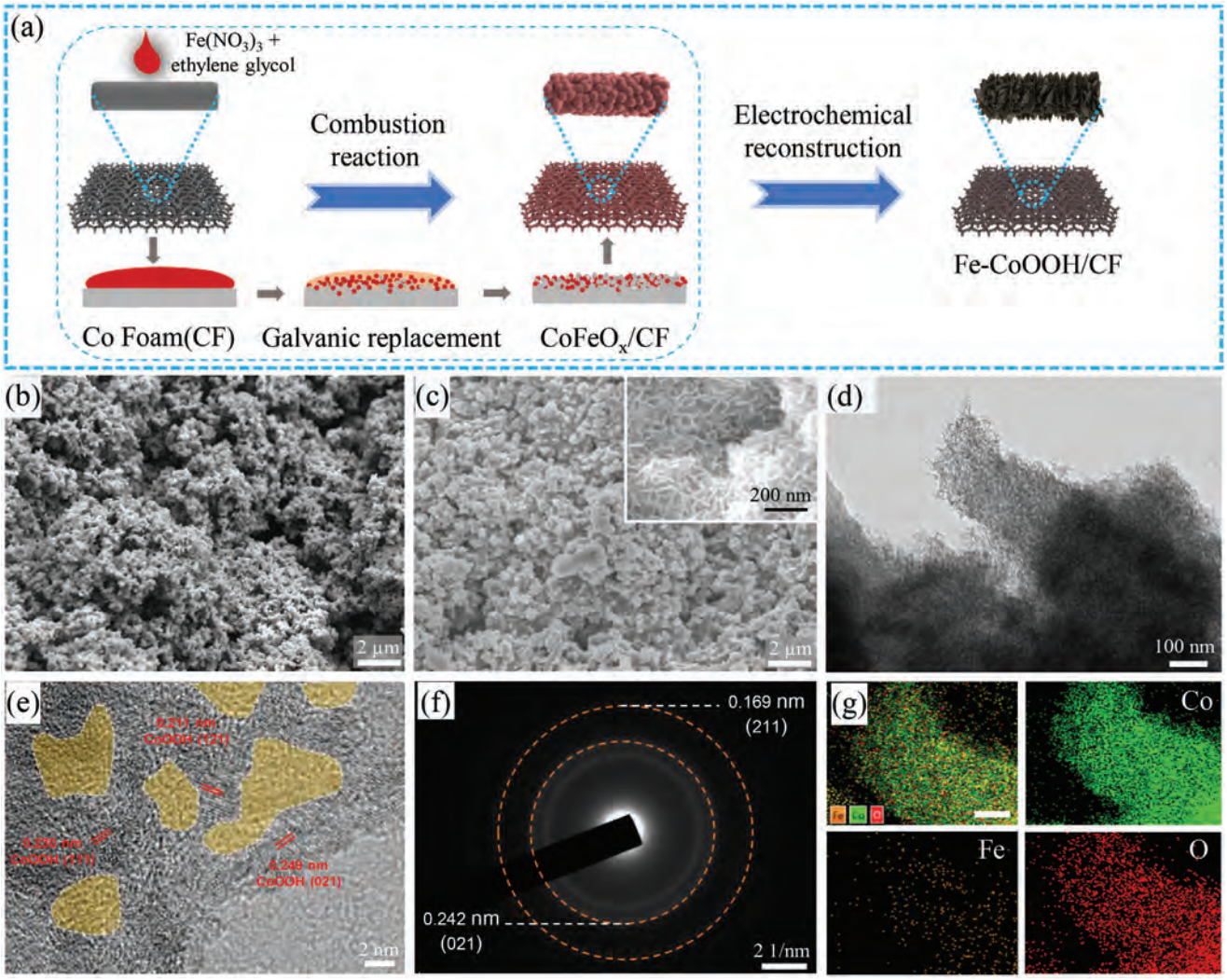

Figure 1. a) Schematic of the synthesis process of Fe-CoOOH/CF electrocatalyst, b) SEM image of the $CoFeO_x$/CF pre-catalyst, c) SEM, d) TEM, e) HR-TEM, and f) SAED images, and g) TEM-EDS mapping of the reconstructed Fe-CoOOH/CF sample taken after the 48-h CP test. The bars in (g) represent 100 nm. The yellow regions in (e) show the amorphous regions.

the CoOOH structure (Figure 1g; Figure S3, Supporting Information). The Co/Fe ratio in the TEM-EDS elemental composition shows ≈1.5% Fe concentration in the Fe-CoOOH/CF structure, which is lower than that of the pre-catalyst, as some of the Fe atoms leach to the electrolyte during reconstruction (Figures S4,S5, Supporting Information).

Electrocatalysts may transform under OER conditions, and these transformations are sometimes detrimental to the activity and stability of the catalysts and not desirable. However, if properly designed, the results can be appealing. Co-based oxide catalyst usually transforms to $CoOOH/Co(OH)_2$, which is an efficient electrocatalyst, but suffers from low activity and poor stability, particularly at high current densities. Iron doping of Co-based hydroxide ($CoOOH/Co(OH)_2$) produces great benefits. Hence, we aim to transform the raw CF substrate into a highly active Fe-CoOOH electrocatalyst by $CoFeO_x$/CF pre-catalyst synthesis and electrochemical surface reconstruction (**Figure** 2a). Two kinds of reconstruction are observed in our study: the quick chemical change of the $CoFeO_x$ to Fe-CoOOH catalyst, and the slow morphological reconstruction of the surface to nanosheets. First, to examine the rapid chemical surface changes and their effect on OER, CV tests are conducted in the potential range (0.8–1.65 V vs RHE). Compared to the first CV cycle, the OER activity of the $CoFeO_x$/CF sample accelerates in the second CV cycle, and then stays constant for the next 50 CV cycles, suggesting that just two CV cycles are required for the sample to accomplish surface activation and maximum activity (Figure S6, Supporting Information). As shown in Figure 2a, a broad and obvious oxidation peak at ≈1.2 V (vs RHE) associated with the Co^{2+}/Co^{3+} transition appears in the first CV scan becomes significantly weaker in the second, and remains unchanged in subsequent CV cycles. This behavior unveils that the quick chemical surface reconstruction process from $CoFeO_x$ to Fe-CoOOH is mostly achieved in the first CV cycle. This transformation leads to an initial high oxidation current density due to the activation of Co^{2+} sites. In the subsequent CV cycles the current density decreases, as most of the

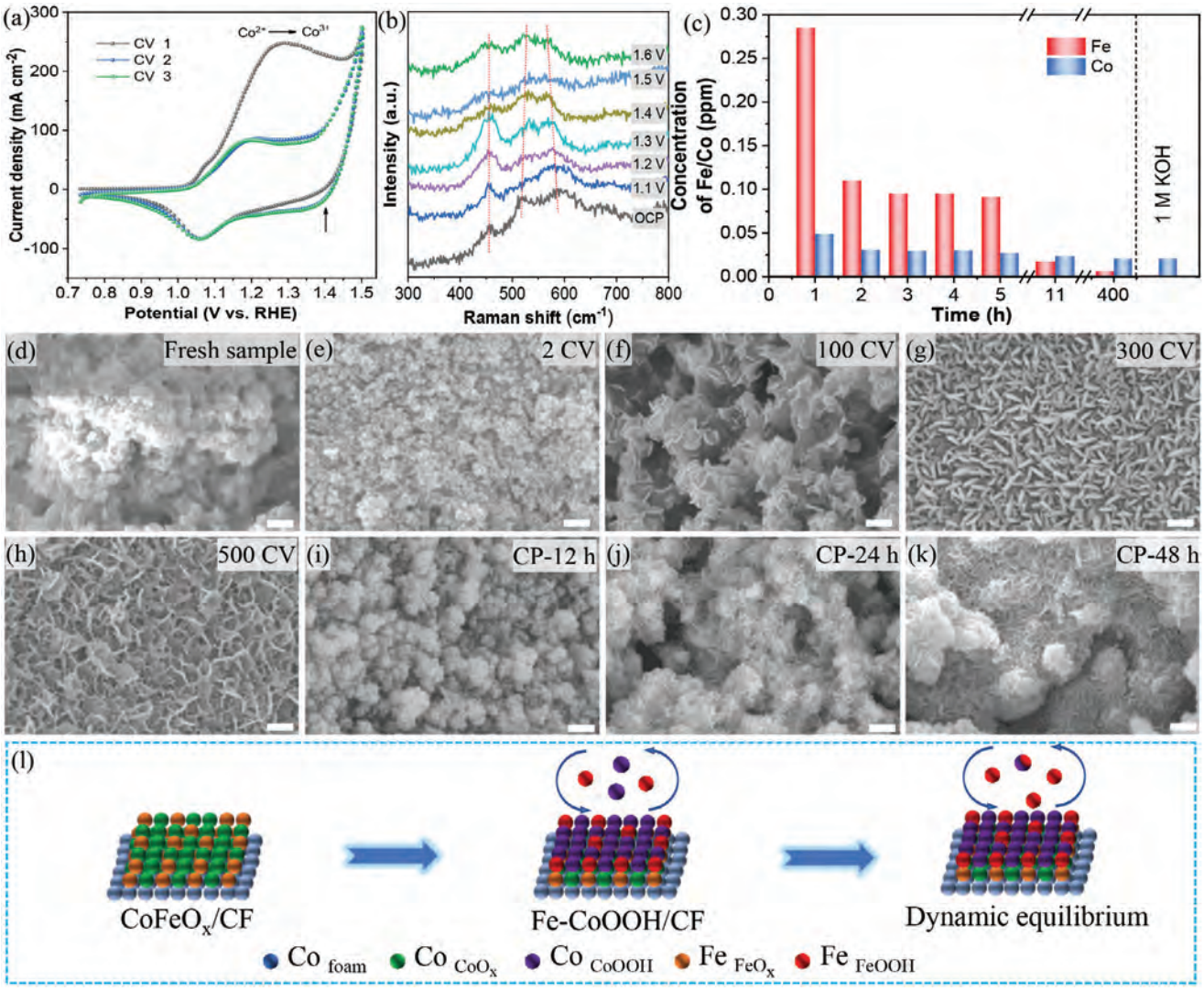

Figure 2. a) CV curves of the $CoFeO_x$/CF pre-catalyst showing the rapid surface reconstruction; b) In situ Raman data showing the surface changes $CoFeO_x$/CF pre-catalyst during OER; c) ICP data of Co, Fe concentration in KOH electrolyte during the OER at different times, showing the leaching effect of Fe from Fe-CoOOH/CF sample; d–h) SEM images showing the surface reconstruction of the $CoFeO_x$/CF precatalyst using CV tests; i–k) SEM images showing the surface reconstruction of $CoFeO_x$/CF precatalyst using CP tests; l) Schematic demonstration of the reconstruction process of the Fe-CoOOH/CF electrocatalyst. The scale bars represent 200 nm.

Co^{2+} on the surface has changed to Co^{3+} in the first cycle. Importantly, the onset potential for the oxidation remains consistent at ≈1.05 V versus RHE throughout the CV cycles. This stability indicates that the fundamental electrochemical processes are preserved despite the observed shifts in peak intensity. This characteristic shows that the $CoFeO_x$/CF pre-catalyst experienced an irreversible chemical surface reconstruction.[16] The rapid surface reconstruction of the $CoFeO_x$/CF pre-catalyst is also confirmed by in situ Raman spectroscopy (Figure 2b). The in situ Raman data are recorded from the sample at the open circuit potential (OCP) and OER at different potentials. Compared to the data at OCP, the peak at 456.7 cm^{-1} related to the Co—O bond of Co_2O_3 fluctuates with increasing applied potentials. Additionally, the peaks at 518.8 and 592.0 cm^{-1} gradually move to higher and lower wavelengths, respectively, showing the surface reconstruction of pre-catalyst and generation of CoOOH/FeOOH species.[17] Interestingly, there is one common phenomenon in these peaks. The peak intensity continuously fluctuates, suggesting dynamic surface reconstruction and active site generation. To further confirm this hypothesis, we investigate the existence of Co/Fe metal ions in the KOH electrolyte at different periods using inductively-coupled plasma optical emission spectroscopy (ICP-OES), as it is a common observation that metal ions leach into the electrolyte during electrochemical reconstruction.[8c,18] As shown in Figure 2c, the ICP-OES data of the KOH electrolyte collected after different intervals of OER reveal that maximum Co/Fe leaching and surface reconstruction of the pre-catalyst occur in the first hour. The leaching of the Co ions from the surface ceases during the second hour, whereas Fe significantly decreases after 10 h. This suggests that the surface undergoes significant

restructuring in the first 10 h and after equilibrium is established between the leaching and redeposition of the Fe ions on the surface. To further support this argument, the metal ion concentration in the electrolyte is determined during the 100 h (300–400 h) operation of the long-term CP test (Figure 2c). The results confirm that Co leaching is terminated while a small amount of Fe is detected. The permanent presence of a small amount of Fe and the appearance and disappearance of the in situ Raman peaks support the existence of dynamic surface reconstruction and active site generation.[18a,19]

The slow morphological surface reconstruction of the $CoFeO_x$/CF pre-catalyst is investigated by SEM and its effect on OER is studied. The effect of CV on the morphology and OER activity reveals a slow generation of nanosheets on the surface, and complete surface reconstruction can be achieved after 500 CV cycles (Figures 2d–h). The CV effect on the OER activity shows that the maximum OER activity is attained in the second CV cycle, and no obvious change is observed in the subsequent 50 cycles (Figure S6, Supporting Information). After the long-term CV experiment (500 cycles), the nanosheets become denser and thinner, but the OER activity slightly decreases (Figure S7, Supporting Information). The surface transformations are also investigated by the CP test. The surface of the pre-catalyst completely changes to Fe-CoOOH nanosheets after 48 h of activity (Figures 2i–k). Likewise, in CV, the sample quickly reaches its peak OER activity and afterward becomes independent of surface variations and maintains its excellent stability. This observation also supports the dynamic active site generation, as once the surface transforms to Fe-CoOOH electrocatalyst, the activity does not decay because of the continuous updating of active sites. Conversely to the CV test, the generation of nanosheets is less after the CP test (48 h), but the activity remains unchanged. This concludes that the CV and CP operations have different effects on morphology and stability. The CV test obtained more populated nanosheets than the CP test, but its electrochemical stability decreases after 500 CV cycles, whereas the stability in the CP test remains stable. In the CV test, the sample undergoes repeated oxidation-reduction cycles of the metal ions, whereas in the CP analysis, it only experiences the oxidation potential. These repeated oxidation-reduction cycles of the metal ions in the CV test can lead to structural and chemical changes, which can negatively impact the activity. To further clarify the advantageous effect of Fe-doping on surface reconstruction and OER activity, undoped CoOOH, and Ni and Cu-doped CoOOH samples are also fabricated by the same method. Compared to the undoped and Ni, Cu-doped sample, Fe doping significantly increases the current density in the non-Faradic region, which is assigned to the surface reconstruction (Figure S8a, Supporting Information). Moreover, Fe-doping shifts the onset of the CV to a much lower potential compared to CoOOH and Ni, Cu-doped samples, revealing that Fe greatly eases the reconstruction process thereby accelerating the OER process (Figure S8a–c, Supporting Information). Combining the SEM/TEM, CV, CP, in situ Raman, and ICP data, it can be concluded that surface reconstruction of the $CoFeO_x$/CF pre-catalyst to Fe-CoOOH/CF electrocatalyst occurs, whereas as a minute amount of the Fe leaching into the electrolytes continuously updates the surface to Co(Fe)OOH active species, as demonstrated in Figure 2l. Moreover, Fe plays a vital role in facilitating surface reconstruction and enhancing the OER activity and durability.

The OER properties of the as-fabricated Fe-CoOOH/CF electrode are examined in a three-electrode system in 1M KOH solution. For comparison, the OER activities of the CoOOH/CF, commercial RuO_2/CF, and Co foam are also investigated. A similar method like the Fe-CoOOH/CF electrode is employed to prepare the CoOOH/CF catalyst except using the $Co(NO)_3.6H_2O$ salt instead of $Fe(NO_3)_3{\bullet}9H_2O$. The CoOOH/CF catalyst has a similar morphology, semi-crystalline nature, and short-range ordering characteristics as the Fe-CoOOH/CF sample (Figure S9, Supporting Information). As shown in **Figure 3a**, the $CoFeO_x$/CF pre-catalyst electrode undergoes an in situ surface reconstruction/activation process and transforms to a semi-crystalline Fe-CoOOH/CF electrocatalyst under OER conditions. The activation process can be achieved very quickly, and the sample can reach its maximum capacity within 2 CV cycles. No obvious changes are observed in subsequent operations up to 50 CV cycles. As expected, the OER polarization curve of the Fe-CoOOH/CF electrode exhibits outstanding characteristics higher than those of CoOOH/CF, benchmark RuO_2/CF, and CF electrocatalysts (Figure 3b). To exclude the impact of the Co^{2+}/Co^{3+} and Co^{3+}/Co^{4+} oxidation process on the catalytic current, linear sweep voltammetry (LSV) is scanned from the positive to the negative direction of the potential. The Fe-CoOOH/CF electrode has excellent water oxidation activities at large current densities, demonstrated by the η of 271 and 291 mV at j of 500 and 1000 mA cm^{-2}, respectively, which are lower than that of the CoOOH/CF, RuO_2/CF, and CF electrodes. Impressively, compared to the RuO_2/CF electrodes, the potential required to achieve j of 1000 mA cm^{-2} is reduced by ≈ 36% (167 mV) by the Fe-CoOOH/CF electrocatalyst. The corresponding Tofel slopes of the OER curve are investigated and Fe-CoOOH/CF (35.6 mV dec^{-1}) sample shows a smaller slope than that of CoOOH/CF (40.1 mV dec^{-1}), RuO_2/CF (87.7 mV dec^{-1}) and CF (90.2 mV dec^{-1}) electrodes, suggesting accelerated OER kinetics and advantageous industrial application potential of Fe-CoOOH/CF (Figure 3c). Moreover, the electrocatalyst outperforms RuO_2/CF at low as well as high current densities and the Tafel plots also unveil the best kinetics (Figure 3d).

The Nyquist plots acquired by electrochemical impedance spectroscopy (EIS) and fitted to an equivalent circuit model further show that Fe-CoOOH/CF (0.19 Ω) electrocatalyst has significantly lower charge transfer resistance than CoOOH/CF (0.89 Ω), RuO_2/CF (0.35 Ω), and CF (2.73 Ω), corroborating its excellent conductivity and suitable OER dynamics (Figure 3e). The electrochemical double-layer capacitance (C_{dl}), which is directly related to the electrochemical surface area, is investigated by cyclic voltammetry. As shown in Figure 3f and Figure S10 (Supporting Information), the C_{dl} of Fe-CoOOH/CF (5.23 mF cm^{-2}) is 6.8 and 2.9 times higher than the RuO_2/CF (0.76 mF cm^{-2}) and CoOOH/CF (1.77 mF cm^{-2}) catalysts, respectively, demonstrates superior intrinsic OER activities and much higher exposed surface-active sites. The capability of the Fe-CoOOH/CF sample to generate high-density active sites makes a crucial contribution to the superior intrinsic OER activity of the electrode. The excellent activities are further confirmed by multicurrent chronopotentiometry recorded from 100 to 1000 mA cm^{-2}. The data are in good agreement with the LSV curve and sustain the

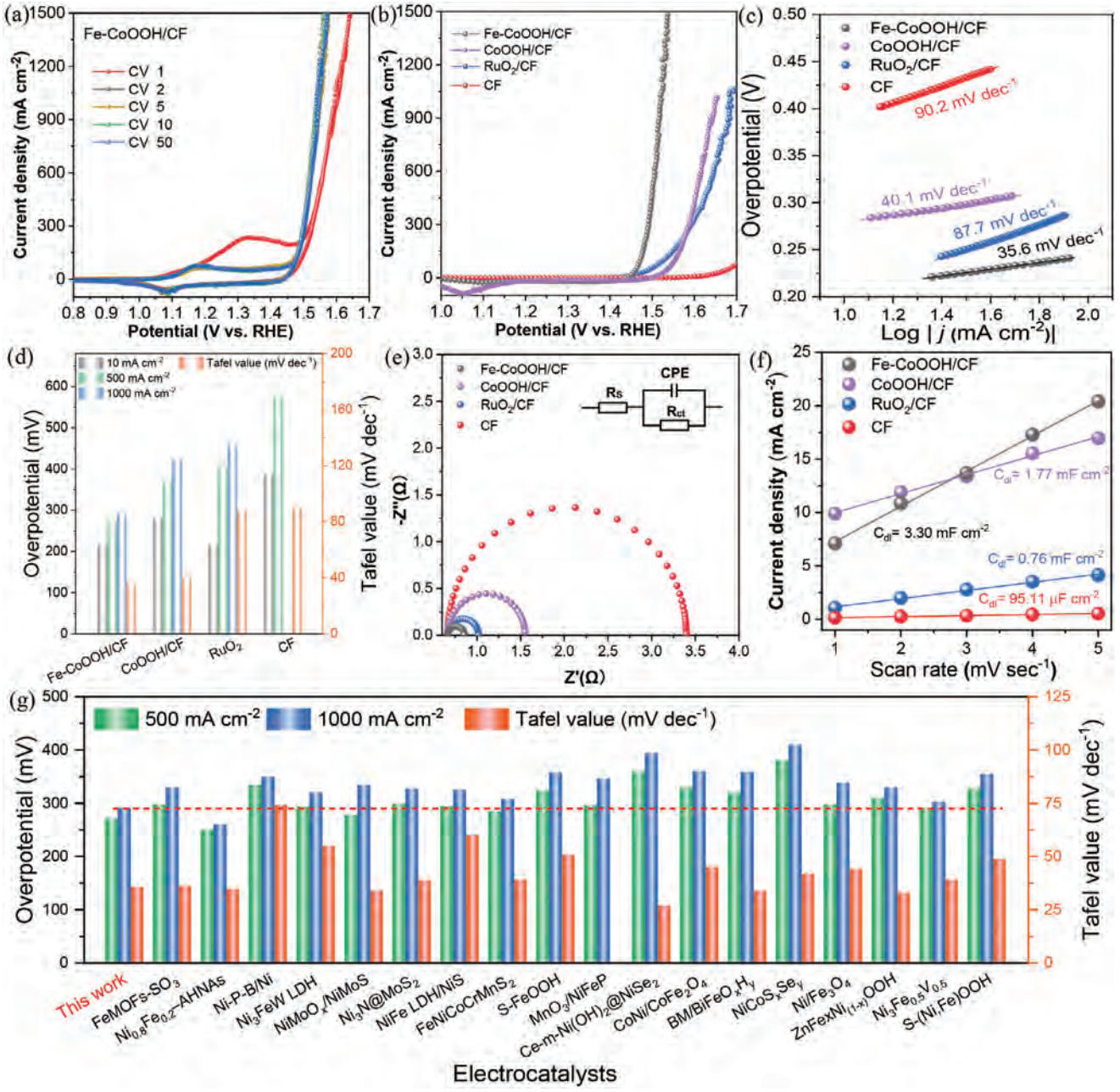

Figure 3. a) CV activation of the $CoFeO_x$/CF pre-catalyst; b) LSV curves of the Co(Fe)OOH electrocatalyst, commercial RuO_2/CF and bare CF (iR-corrected); c) Corresponding Tafel slopes of OER; d) Comparison of the overpotential at different *j* and Tafel values; e) EIS data and f) ECSA of the Fe-CoOOH/CF, CoOOH/CF, RuO_2/CF and CF samples; g) Comparison of the OER performances of Fe-CoOOH/CF sample and state-of-the-art reported electrocatalysts having j_{HCD} (≥1000 mA cm^{-2}).

high activity and mechanical robustness of the Fe-CoOOH/CF electrocatalyst (Figure S11, Supporting Information). The significance of the Fe doping is further studied by doping the CoOOH catalyst with other transition metal metals. In addition to easing the reconstruction process, Fe better enhances the OER activity, and reduces the charge transfer resistance, compared to Ni, Cu doping (Figure S8b,c, Supporting Information). We believe that the OER performance reported in this study is among the best demonstrated in water oxidation electrolyzers, particularly at j_{HCD} ≥1000 mA cm^{-2}, as compared with recently reported benchmark electrocatalysts having j_{HCD} and synthesized on foamy substrates (Figure 3g and Table S1, Supporting Information). The OER performance of Fe-CoOOH/CF is comparable with or even superior to the benchmark j_{HCD} electrocatalysts reported to date. The reproducibility of a method is of utmost importance for real-life applications. Therefore, we synthesize five samples by the same method and examine the OER activities. The samples have very similar OER properties, demonstrating

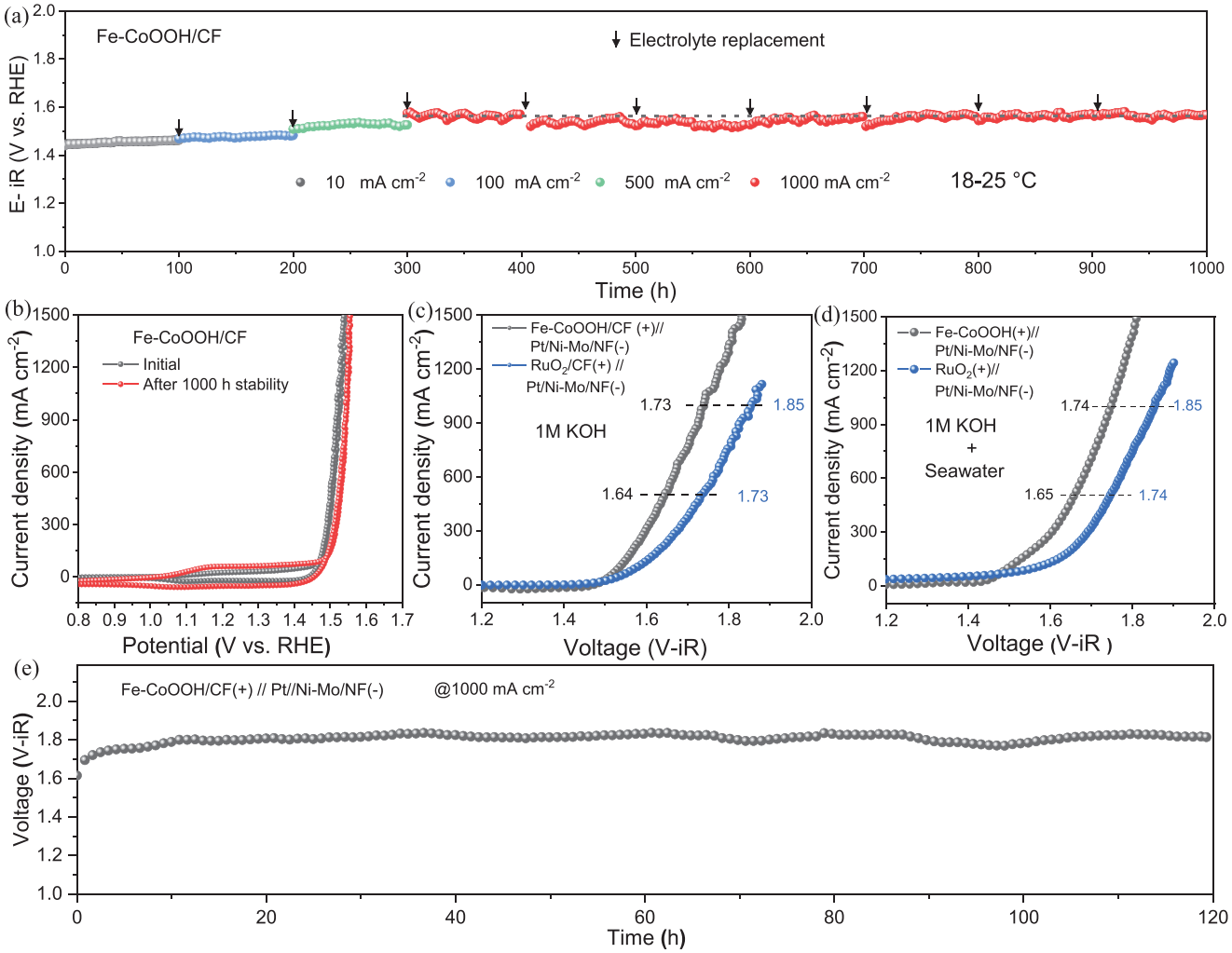

Figure 4. a) Long-term stability testing of Fe-CoOOH/CF electrocatalyst at different *j*; b) CV curves of the Fe-CoOOH/CF electrocatalyst before and after long-term stability test; c,d) Comparison of the water splitting properties of the Fe-CoOOH/CF(+)//Pt/Ni-Mo/NF (−) electrolyzer with those of the benchmark RuO_2/NF(+)//Pt/Ni-Mo/NF (−) electrolyzer in 1 M KOH; and 1 M KOH + seawater. e) Stability test of the Fe-CoOOH/CF(+)//Pt/Ni-Mo/NF (−) electrolyzer pair in water splitting at j_{HCD} of 1000 mA cm^{-2} in 1 M KOH.

excellent repeatability (Figure S12, Supporting Information). The effect of the amount of the precursor solution on OER is also optimized, and 100 µL cm^{-2} delivers the best performance (Figure S13, Supporting Information).

One of the important factors that determine the possibility of an electrocatalyst in industrial applications is its stability at elevated current density (≥500 mA cm^{-2}). First, we examine the stability of the Fe-CoOOH/CF sample at *j* of 10 mA cm^{-2} for a single run up to 100 h, and the results show a negligible decrease (**Figure** 4a). Next, we increase the current density to 100 mA cm^{-2} and continue for another 100 h. Impressively, the sample still maintains its excellent stability. From a commercial point of view, the large current density is pivotal. Hence, the Fe-CoOOH/CF electrocatalyst is employed to carry out OER operation at j of 500 mA cm^{-2} for another 100 h, showing remarkable stability and stable current output. Finally, to reveal the real industrial application potential of the as-fabricated Fe-CoOOH/CF electrode, the sample undergoes a durability test at a practical j_{HCD} of 1000 mA cm^{-2}. As shown in Figure 4a (brown line), the catalyst demonstrates exceptional durability and operates at 1000 mA cm^{-2} for a long duration of 700 h without any decay. The fluctuation in the current density is due to the variation in temperature (18–25 °C) during the test, as OER is carried out in a partially controlled environment. The outstanding stability is further confirmed by the LSV curve obtained after the long OER operation. The initial and after 1000 h LSV curves show a negligible decrease in the activity (Figure 4b). The outstanding stability of the catalyst can be attributed to the synergistic cooperation of the Fe-CoOOH species and dynamically active $Fe(OH)_2$/FeOOH species as well as the continuous update of Fe-active sites during dynamic equilibrium. As discussed in the previous section, after the completion of the reconstruction process and generation of the FeOOH, Fe-CoOOH active sites on the surface, a very small amount of Fe dissolves and establishes a dynamic and robust catalytic interface. The SEM images taken after the 1000 h CP test display that the morphology of the sample changed slightly

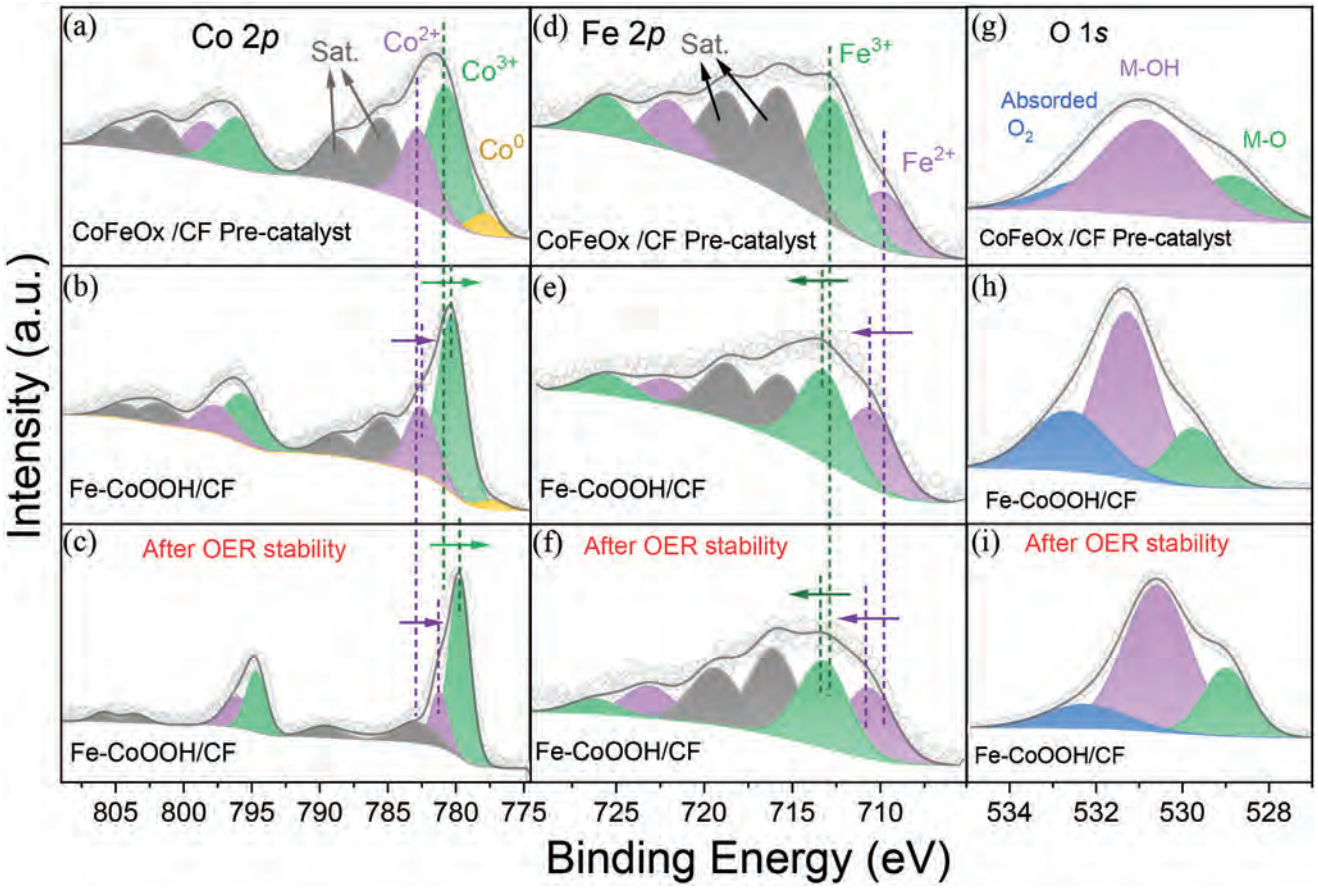

Figure 5. High-resolution XPS spectra of (a,b,c) Co 2p, (d,e,f) Fe 2p, and (g,h,i) O 1s of the (a,d,g) $CoFeO_x$/CF pre-catalyst, (b,e,h) Fe-CoOOH/CF after 48-h reconstruction, and (c,f,i) Fe-CoOOH/CF after the long 1000-h OER test.

(Figure S14, Supporting Information). This slight alteration may arise due to the continuous replacement of the electrolyte after each 100 h operation where a small amount of Fe leaches to develop the dynamic reconstruction process and to maintain the equilibrium between leaching and redeposition of Fe.

Industrial water splitting is always operated in a two-electrode system, which is more feasible and simpler. Inspired by the remarkable OER performance, we further evaluate the capability of the as-synthesized Fe-CoOOH/CF anode in a two-electrode set-up and couple it with a Pt/Ni-Mo/NF cathode for overall water splitting. The Pt/Ni-Mo/NF HER electrocatalyst is prepared following a reported method[20] and the HER performance is provided in Figure S15 (Supporting Information). Impressively, robust catalytic performance is accomplished by the Fe-CoOOH/CF(+)//Pt/Ni-Mo/NF (−) electrolyzer pair, requiring low cell voltages of 1.48, 1.53, 1.64, and 1.74 V at j of 10, 100, 500, and 1000 mA cm^{-2}, respectively (Figure 4c). To further demonstrate the importance of the Fe-CoOOH/CF sample as an efficient OER catalyst, the commercial RuO_2/CF electrocatalyst is coupled with Pt/Ni-Mo/NF cathode and its water splitting activity is examined (Figure 4c). Compared to RuO_2/CF(+)//Pt/Ni-Mo/NF (−) electrolyzer pair, the Fe-CoOOH/CF(+)//Pt/Ni-Mo/NF(−) electrolyzers deliver dominant performances. To further verify the outstanding two-electrode performance, multicurrent chronopotentiometry is carried out from 100 to 1000 mA cm^{-2}, and the results match the LSV data (Figure S16, Supporting Information). The possibility of employing the Fe-CoOOH(+)//Pt/Ni-Mo/NF(−) electrolyzer in alkaline seawater is also tested (Figure 4d). Encouragingly, the catalytic couple affords 500 and 1000 mA cm^{-2} at low cell voltages of 1.65 and 1.74 V, respectively, outperforming the RuO_2/CF(+)//Pt/Ni-Mo/NF(−) couple and rendering it a promising candidate for alkaline seawater splitting. The operational stability, which is a vital parameter, is investigated for Fe-CoOOH(+)//Pt/Ni-Mo/NF(−) couple in the two-electrode system at j_{HCD} of 1000 mA cm^{-2}. The catalytic couple shows good durability up to 120 h with no obvious decline (Figure 4e). To confirm that the current density produced during the electrochemical testing is generated from the water splitting reaction, the Faradic efficiency of the Fe-CoOOH(+)//Pt/Ni-Mo/NF(−) electrolyzers at 100 mA cm^{-2} is investigated. As demonstrated in Figure S17 (Supporting Information), H_2/O_2 is generated with an ideal volume ratio of closely 2:1, and the Faradic efficiency is ≈100% for both H_2/O_2 gas production.

The surface evolution of the $CoFeO_x$/CF pre-catalyst to Fe-CoOOH/CF electrode with a focus on electronic structure and bonding states is monitored by X-ray photoelectron spectroscopy (XPS) (**Figure 5**). The XPS survey spectra of the $CoFeO_x$/CF pre-catalyst and Fe-CoOOH/CF sample after 48-h reconstruction and long 1000-h OER stability test are presented in Figure S18

(Supporting Information). All the samples reveal the presence of Co, Fe, and O. With regard to Co in the pre-catalyst (Figure 5a), the Co $2p_{3/2}$ and Co $2p_{1/2}$ peaks are fitted with binding energies of 780.7/796.2 and 782.8/798.5 eV ascribed to Co^{3+} and Co^{2+}, respectively.[21] The Co^{3+} and Co^{2+} peaks and their corresponding satellite peaks show that the Co in the pre-catalyst is present in the form of inverse spinel Co_3O_4.[22] The gap between the peaks of Co $2p_{3/2}$ and Co $2p_{1/2}$ is more than 15 eV, implying the co-existence of Co^{3+} and Co^{2+} oxidation states.[8b,21] A small peak ≈777.9 eV can be assigned to the Co^0 oxidation state which may arise from the Co foam.[8b] The Fe 2*p* spectrum is deconvoluted into two pairs of $2p_{3/2}/2p_{1/2}$ peaks at 709.9/722.1 eV and 712.8/725.7 corresponding to Fe^{2+} and Fe^{3+} species (Figure 5d)[14c], respectively. The peaks at 715.8 and 718.9 eV represent the respective satellite peaks of Fe^{2+} and Fe^{3+}. The O 1*s* spectrum of the $CoFeO_x$/CF pre-catalyst consists of three peaks positioned at 528.8, 530.8, and 532.1 eV and can be assigned to the M—O, M—OH bonds and adsorbed oxygen (Figure 5g).

The Co 2*p* peaks of the reconstructed Fe-CoOOH/CF sample (Figure 5b) and after the long OER stability test (Figure 5c) become sharper, and the peaks representing Co^{3+} and Co^{2+} move to lower binding energy, suggesting the change in the chemical environment of the surface and generation of CoOOH and $Co(OH)_2$ electrocatalyst.[8b,c] Compared to the peaks of Co^{2+}, the intensity of the Co^{3+} species increases with continuous OER operation (Figure 5b,c), showing that the surface is mostly transformed to CoOOH electrocatalyst.[6b] Moreover, the intensity of the peaks associated with Co^0 decreases after the reconstruction process and disappears entirely after long-term stability testing. Furthermore, the noticeable shift in Fe 2p peaks to higher binding energies, corresponding to Fe^{2+} and Fe^{3+}, substantiates the formation of FeOOH and $Fe(OH)_2$ species. The presence of these surface-active $Fe(OH)_2$/FeOOH species demonstrates their important contribution to the OER process (Figures 5e,f).[14c,18b] The O 1*s* peak of the reconstructed Fe-CoOOH/CF sample can be divided into three peaks at 529.7, 531.2, and 532.6 eV corresponding to M—O, M—OH, and adsorbed O_2 (Figure 5g).[23] The O 1*s* peaks also become sharper after reconstruction, indicating the changes in the surrounding chemical bonding (Figure 5h). Meanwhile, the ratio of the O 1*s* peak at 528.9 eV associated with M—O increases after the OER stability test, revealing the dynamic surface changes at the interface and further supporting the dynamic active site generation (Figure 5i). These findings from the XPS combined with the in situ Raman, SEM/TEM images and ICP data suggest that the FeOOH and $Fe(OH)_2$ active species play an important role alongside Fe-CoOOH, in enhancing the overall catalytic performance and stability of the Fe-CoOOH/CF catalyst. This comprehensive understanding aligns with the observed data and provides deeper insights into the underlying mechanisms driving the catalyst's high efficiency and durability.

To gain further insights into the enhanced OER performance of the Fe-CoOOH catalyst, theoretical investigations are performed based on the computational standard hydrogen electrode model coupled with the self-consistent theoretical overpotential method.[24,25] To better identify the OER active species and to shed light on the capability of doping to influence the electronic structure and adsorption ability of the CoOOH sample, we examine the OER activity of CoOOH, $Fe_xCo_{1-x}OOH$, $Ni_xCo_{1-x}OOH$, and $Cu_xCo_{1-x}OOH$ (**Figure 6a**). Additionally, we explore an alternative scenario where the dopant metal tends to adsorb onto the CoOOH surface, forming Fe-CoOOH, Ni-CoOOH, and Cu-CoOOH. The CoOOH surface exposes two types of local atomic environments where the metal dopant can bind, referred to as site A and site B, as depicted in Figure 6b. The calculated binding energy for each metal on the CoOOH surface indicates that site A is more favorable for stabilizing the metal. The binding energy for Fe, Ni, and Cu at site A is ≈−2.37, −1.68, and −1.22 eV, respectively, while the binding energy decreases to −1.92, −1.09, and −0.88 eV, respectively, at site B. Consequently, we proceed with the OER investigation focusing on the OER performance with the metal adsorbed at site A.

For a better understanding of the stability of the metal dopant on CoOOH and its electronic properties, we examine the projected density of states (pDOS) of various metals on CoOOH sites. As depicted in Figure 6c, Fe-CoOOH exhibits a higher DOS near the Fermi level compared to Ni-CoOOH and Cu-CoOOH. It is well-known that high electron densities near the Fermi level can enhance the adsorption of OER intermediates. Similarly, for the CoOOH, $Fe_xCo_{1-x}OOH$, $Ni_xCo_{1-x}OOH$, and $Cu_xCo_{1-x}OOH$ sites, $Fe_xCo_{1-x}OOH$ demonstrates a higher DOS near the Fermi level than the other sites, indicating the increased reactivity to the intermediates (Figure S19, Supporting Information). Furthermore, the calculated crystal orbital Hamilton population (COHP) for Fe—CoOOH, Ni—CoOOH, and Cu—CoOOH reveals a strong bonding near the Fermi energy for Fe—CoOOH in comparison to Ni—CoOOH and Cu—CoOOH (Figure S20, Supporting Information), suggesting its relatively higher stability and promising high charge transfer.

Subsequently, we delve into the atomic-scale mechanism of OER on the CoOOH, $Fe_xCo_{1-x}OOH$, $Ni_xCo_{1-x}OOH$, and $Cu_xCo_{1-x}OOH$ sites, as illustrated in Figure 6d. The calculated overpotentials are 0.73, 0.48, 1.41, and 1.22 V for CoOOH, $Fe_xCo_{1-x}OOH$, $Ni_xCo_{1-x}OOH$, and $Cu_xCo_{1-x}OOH$, respectively. The oxidation of $^*OOH$ to O_2 is identified as the potential-limiting step for CoOOH and $Fe_xCo_{1-x}OOH$, while the oxidation of $^*OH$ to $^*O$ is the potential-limiting step for $Ni_xCo_{1-x}OOH$, and $Cu_xCo_{1-x}OOH$. This observation can be attributed to the strong binding between $^*OOH$ and the CoOOH and $Fe_xCo_{1-x}OOH$ sites, as well as the low adsorption energy of $^*OH$ intermediate on $Ni_xCo_{1-x}OOH$, and $Cu_xCo_{1-x}OOH$. Additionally, the poor tendency of $Ni_xCo_{1-x}OOH$ and $Cu_xCo_{1-x}OOH$ to be oxidized makes the formation of $^*O$ intermediate challenging. However, as shown in Figure 6e, the adsorption of Ni and Cu on the CoOOH surface significantly alters the binding of the intermediates and weakens the $^*OH$, $^*O$, and $^*OOH$ adsorption energies compared to those on $Ni_xCo_{1-x}OOH$, and $Cu_xCo_{1-x}OOH$. Consequently, the calculated theoretical overpotentials decrease to 1.16 and 0.93 V on Ni and Cu metal sites, respectively, while the calculated overpotential for Fe-CoOOH increases to ≈1.57 V, due to the high adsorption energy of the $^*OOH$ intermediate. These results suggest that the modulation of metal site OER activity is strongly linked to the local atomic environment. Because of the harsh conditions of OER, we assume that the Fe-CoOOH undergoes oxidation during the reaction. Consequently, we investigate the structural stability of Fe-CoOOH with varying oxidation levels at the specified electrode potential. As shown in Figure 6f, we construct surface Pourbaix diagrams for Fe-CoOOH with different OH^* and O^* coverages. Our observations

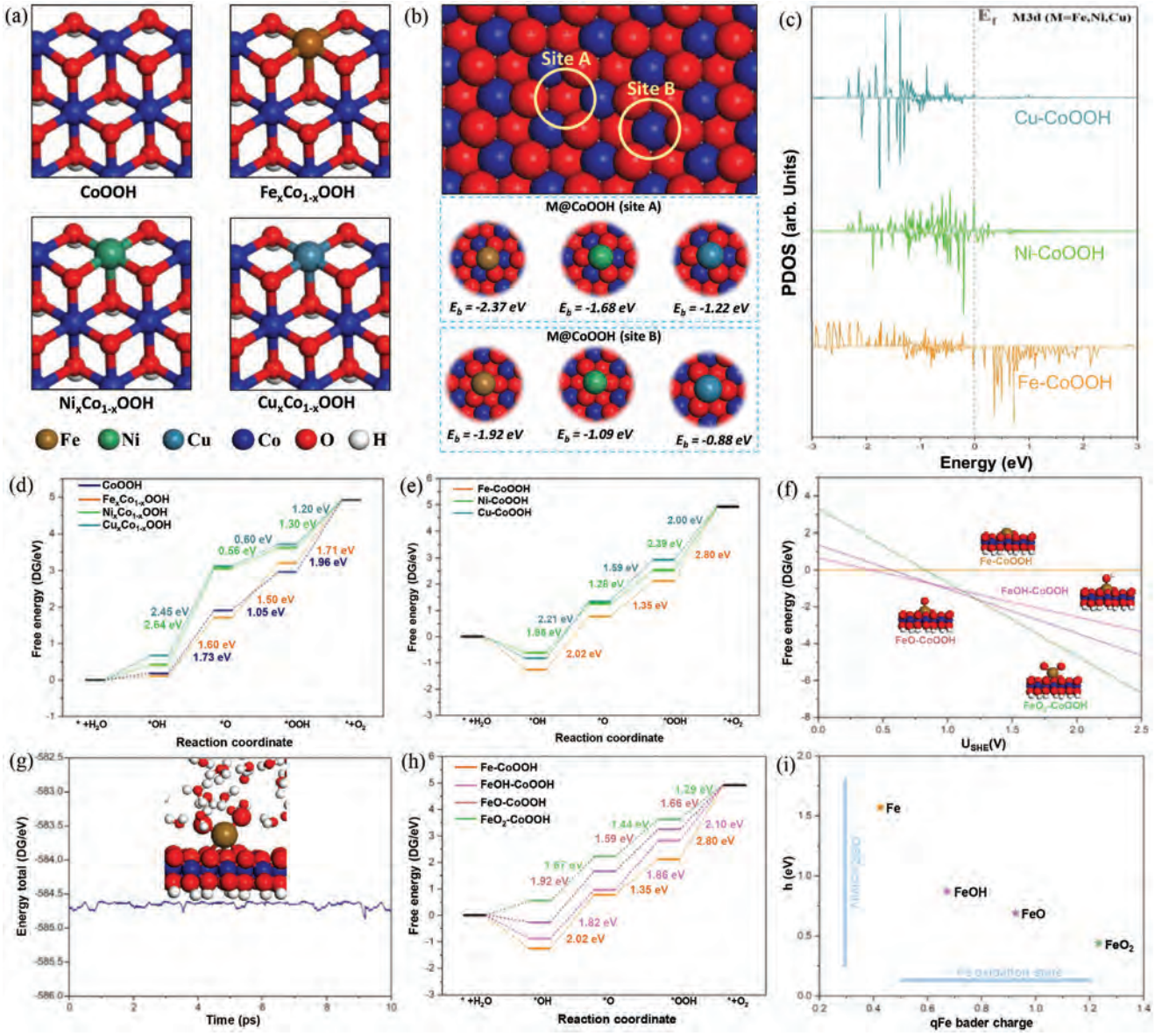

Figure 6. a) Optimized structures and binding energy of Fe, Ni, and Cu atoms anchored on different sites of CoOOH surface; b) Optimized structures of CoOOH and its derivatives doped with Fe, Ni, and Cu, c) Fe, Ni, and Cu 3*d* projected density of states (PDOS) in Fe-CoOOH, Ni-CoOOH, and Cu-CoOOH; d) Free energy diagrams of OER on CoOOH, $Fe_xCo_{1-x}OOH$, $Ni_xCo_{1-x}OOH$ and $Cu_xCo_{1-x}OOH$; e) Free energy diagrams of OER on Fe-CoOOH, Ni-CoOOH, and Cu-CoOOH; f) Pourbaix diagram of the stability for oxidized Fe-CoOOH surfaces us function electrode potential at pH = 0; g) Molecular Dynamic simulation of FeO_2-CoOOH in presence of water solvent; h) Free energy diagrams of OER on oxidized Fe-CoOOH surfaces; i) Correlation between potential determining step (PDS) and the Fe bader charge.

indicate that at low electrode potentials, Fe-CoOOH may exist in the forms of FeO-CoOOH or FeOH-CoOOH. Conversely, at a high electrode potential (U ≈ 1.20 V), Fe-CoOOH tends to oxidize, forming the FeO_2-CoOOH structure. This suggests the formation of a metal oxide, potentially destabilizing the metal on the CoOOH surface. Subsequently, we assess its stability through a 10 ps molecular dynamic simulation in the presence of water solvent, as shown in Figure 6g. The results demonstrate the relative stability of the newly formed FeO_2-CoOOH structure, indicating its likely existence under real working conditions. Next, we delve into the energy profile of OER on Fe-CoOOH and the derivative oxidized structures, namely FeOH-CoOOH, FeO-CoOOH, and FeO_2-CoOOH, as illustrated in Figure 6h. Notably, the calculated overpotentials exhibit a significant decrease to 0.87, 0.69, and 0.44 V for FeOH-CoOOH, FeO-CoOOH, and FeO_2-CoOOH, respectively. It is worth noting that the oxidation of *OH to *O represents the potential limiting step for FeO-CoOOH and FeO_2-CoOOH. It appears that the oxidation of metal sites contributes to the enhanced OER activity. This is supported by the Bader charge calculation for the metal site, as depicted in Figure 6i, where the oxidation state correlates with the OER activity. In other words, a higher Fe oxidation state maximizes the OER activity. This can

be explained by the fact that Fe has an affinity for oxygenating intermediates (*OH, *O, and *OOH), making them highly adsorbed to Fe, resulting in high overpotentials. Conversely, when Fe is at a high oxidation state, the affinity for oxygenating intermediates decreases, leading to moderate adsorption energy of OER reaction intermediates. Figure S21a,b (Supporting Information) represent the possible OER mechanism on FeO_2-CoOOH and $Fe_xCo_{1-x}OOH$, respectively. Overall, according to the DFT investigation, it can be concluded that both sites are active in the OER reaction, with a slight superiority for the Fe sites exposed on the CoOOH surface.

3. Conclusion

A rapid and cost-effective method is designed to fabricate the self-standing, active, and ultra-stable Fe-CoOOH/CF electrocatalyst for OER in alkaline electrolytes. The solution combustion method is used to grow $CoFeO_x$ nanoparticles by steering raw CF, while the reconstruction of the pre-catalyst to Fe-CoOOH/CF is carried out in situ under electrochemical OER conditions. A small amount of Fe leaching establishes the dynamic surface reconstruction to update the surface-rich $FeOOH/Fe(OH)_2$ electrocatalyst. The in situ formed Fe-CoOOH electrocatalyst exhibits superior OER activity with low overpotentials of 271 and 291 mV at current densities of 500 and 1000 mA cm^{-2}, respectively, and long-term operational stability of 1000 h. DFT calculations shed light on the comparative adsorption ability of Fe, Ni, and Cu into CoOOH structure, revealing that Fe doping has greater ability in assisting the reconstruction process, optimizing the adsorption of OER intermediate, and stabilizing CoOOH species by regulating the electronic density. Overall, the Fe-CoOOH/CF electrocatalyst delivers exceptional performance in both the OER and two-electrode water-splitting systems. The outstanding properties are expected to pave the way for large-scale deployment of water electrolysis systems.

Supporting Information

Supporting Information is available from the Wiley Online Library or from the author.

Acknowledgements

A.Q. and K.H. contributed equally to this work. The support from the Guangdong Basic and Applied Basic Research Foundation (2024A1515012127 and 2022A1515240007), National Natural Science Foundation of China (W2433039), and the Special Fund Project for Science and Technology Innovation Strategy of Guangdong Province (STKJ202209077 and STKJ202209083), and City University of Hong Kong Strategic Research Grant (SRG) (Grant No. 7005505) are gratefully acknowledged.

Conflict of Interest

The authors declare no conflict of interest.

Data Availability Statement

The data that support the findings of this study are available from the corresponding author upon reasonable request.

Keywords

cobalt oxyhydroxide, combustion synthesis, long stability, oxygen evolution reaction, surface reconstruction

Received: October 2, 2024
Revised: November 1, 2024
Published online: November 24, 2024

[1] a) M. Klingenhof, H. Trzesniowski, S. Koch, J. Zhu, Z. Zeng, L. Metzler, A. Klinger, M. Elshamy, F. Lehmann, P. W. Buchheister, A. Weisser, G. Schmid, S. Vierrath, F. Dionigi, P. Strasser, *Nat. Catal.* **2024**, https://doi.org/10.1038/s41929-024-01238-w; b) X. Liu, J. Chi, H. Mao, L. Wang, *Adv. Energy Mater.* **2023**, *13*, 2301438; c) M. Rafiq, Z. Huang, C. Pi, L. Hu, F. Lu, K. Huo, P. K. Chu, *Renewables* **2024**, *2*, 2.

[2] a) K. Daehn, R. Basuhi, J. Gregory, M. Berlinger, V. Somjit, E. A. Olivetti, *Nat. Rev. Mater.* **2021**, *7*, 275; b) P. Roy Chowdhury, H. Medhi, K. G. Bhattacharyya, C. M. Hussain, *Coordin. Chem. Rev.* **2024**, *501*, 215547.

[3] a) A. J. Shih, M. C. O. Monteiro, F. Dattila, D. Pavesi, M. Philips, A. H. M. daSilva, R. E. Vos, K. Ojha, S. Park, O. van der Heijden, G. Marcandalli, A. Goyal, M. Villalba, X. Chen, G. T. K. K. Gunasooriya, I. McCrum, R. Mom, N. López, M. T. M. Koper, *Nat. Rev. Methods Primers* **2022**, *2*, 84; b) J. Zhu, L. Hu, P. Zhao, L. Lee, K. Y. Wong, *Chem. Rev.* **2020**, *120*, 851.

[4] a) J. Ren, L. Chen, H. Wang, W. Tian, Z. Yuan, *Energy Environ. Sci.* **2024**, *17*, 49; b) H. Meskher, A. R. Woldu, P. K. Chu, F. Lu, L. Hu, *EcoEnergy* **2024**, https://doi.org/10.1002/ece2.68;

[5] a) M. Rafiq, X. Hu, Z. Ye, A. Qayum, H. Xia, L. Hu, F. Lu, P. K. Chu, *Nano Energy* **2022**, *91*, 106661; b) D. Henkensmeier, W. Cho, P. Jannasch, J. Stojadinovic, Q. Li, D. Aili, J. Jensen, *Chem. Rev.* **2024**, *124*, 6393.

[6] a) N. Zhang, X. Feng, D. Rao, X. Deng, L. Cai, B. Qiu, R. Long, Y. Xiong, Y. Lu, Y. Chai, *Nat. Commun.* **2020**, *11*, 4066; b) J. T. Mefford, A. R. Akbashev, M. Kang, C. L. Bentley, W. E. Gent, H. D. Deng, D. H. Alsem, Y. S. Yu, N. J. Salmon, D. A. Shapiro, P. R. Unwin, W. C. Chueh, *Nature* **2021**, *593*, 67; c) J. Kang, X. Qiu, Q. Hu, J. Zhong, X. Gao, R. Huang, C. Wan, L.-M. Liu, X. Duan, L. Guo, *Nat. Catal.* **2021**, *4*, 1050; d) T. Wu, S. Sun, J. Song, S. Xi, Y. Du, B. Chen, W. A. Sasangka, H. Liao, C. L. Gan, G. G. Scherer, L. Zeng, H. Wang, H. Li, A. Grimaud, Z. J. Xu, *Nat. Catal.* **2019**, *2*, 763.

[7] a) T. Wu, E. Song, S. Zhang, M. Luo, C. Zhao, W. Zhao, J. Liu, F. Huang, *Adv. Mater.* **2022**, *34*, 2108505; b) P. Zhai, Y. Zhang, Y. Wu, J. Gao, B. Zhang, S. Cao, Y. Zhang, Z. Li, L. Sun, J. Hou, *Nat. Commun.* **2020**, *11*, 5462; c) L. Yu, L. Wu, B. McElhenny, S. Song, D. Luo, F. Zhang, Y. Yu, S. Chen, Z. Ren, *Energy Environ. Sci.* **2020**, *13*, 3439.

[8] a) C. Huang, P. Qin, Y. Luo, Q. Ruan, L. Liu, Y. Wu, Q. Li, Y. Xu, R. Liu, P. K. Chu, *Mater. Today Energy* **2022**, *23*, 100911; b) S. Hao, L. Chen, C. Yu, B. Yang, Z. Li, Y. Hou, L. Lei, X. Zhang, *ACS. Energy Lett.* **2019**, *4*, 952; c) R. Fan, Y. Zhou, M. Li, J. Xie, W. Yu, J. Chi, L. Wang, J. Yu, Y. Chai, B. Dong, *Chem. Eng. J.* **2021**, *426*, 131943; d) Z. Xiao, Y. C. Huang, C. L. Dong, C. Xie, Z. Liu, S. Du, W. Chen, D. Yan, L. Tao, Z. Shu, G. Zhang, H. Duan, Y. Wang, Y. Zou, R. Chen, S. Wang, *J. Am. Chem. Soc.* **2020**, *142*, 12087; e) R. Li, H. Xu, P. Yang, D. Wang, Y. Li, L. Xiao, X. Lu, B. Wang, J. Zhang, M. An, *Nano-Micro Lett.* **2021**, *13*, 120; f) W. H. Lee, M. H. Han, Y. J. Ko, B. K. Min, K. H. Chae, H. S. Oh, *Nat. Commun.* **2022**, *13*, 605.

[9] a) N. C. S. Selvam, L. Du, B. Y. Xia, P. J. Yoo, B. You, *Adv. Funct. Mater.* **2020**, *31*, 2008190; b) C. Fan, X. Wu, M. Li, X. Wang, Y. Zhu, G. Fu, T. Ma, Y. Tang, *Chem. Eng. J.* **2022**, *431*, 133829; c) Y. Wang, Y. Zhu, S. Zhao, S. She, F. Zhang, Y. Chen, T. Williams, T. Gengenbach, L. Zu,

H. Mao, W. Zhou, Z. Shao, H. Wang, J. Tang, D. Zhao, C. Selomulya, *Matter* **2020**, *3*, 2124; d) X. Luo, X. Tan, P. Ji, L. Chen, J. Yu, S. Mu, *EnergyChem* **2023**, *5*, 100091.

[10] a) S. Anantharaj, S. Kundu, S. Noda, *Nano Energy* **2021**, *80*, 105514; b) Y. Li, L. Hu, W. Zheng, X. Peng, M. Liu, P. Chu, L. Lee, *Nano Energy* **2018**, *52*, 360.

[11] a) X. Lu, W. Tu, Y. Zhou, Z. Zou, *Adv. Energy Mater.* **2023**, *13*, 2300628; b) Z. Huang, A. R. Woldu, X. Peng, P. K. Chu, Q. Tong, L. Hu, *Chem. Eng. J.* **2023**, *477*, 147155; c) Z. Huang, S. Zhu, Y. Duan, C. Pi, X. Zhang, A. R. Woldu, J. X. Jian, P. K. Chu, Q. Tong, L. Hu, X. Yao, *J. Energy Chem.* **2024**, *89*, 99; d) Z. Huang, P. Li, M. Feng, W. Zhu, A. Woldu, Q. Tong, L. Hu, *Inorg. Chem.* **2024**, *63*, 15493.

[12] a) J. Kang, X. Yang, Q. Hu, Z. Cai, L. M. Liu, L. Guo, *Chem. Rev.* **2023**, *123*, 8859; b) Y. Li, Z. Wu, X. Zhang, F. Song, L. Cao, H. Sheng, X. Gao, C. Li, H. Li, W. Li, B. Dong, *Small* **2022**, *19*, 2206859; c) M. Rafiq, K. Harrath, M. Feng, R. Li, A. R. Woldu, P. K. Chu, L. Hu, L. Lu, X. Yao, *Adv. Energy Mater.* **2024**, https://doi.org/10.1002/aenm.202402866.

[13] a) M. Chatenet, B. G. Pollet, D. R. Dekel, F. Dionigi, J. Deseure, P. Millet, R. D. Braatz, M. Z. Bazant, M. Eikerling, I. Staffell, P. Balcombe, Y. Shao-Horn, H. Schafer, *Chem. Soc. Rev.* **2022**, *51*, 4583; b) J. H. Kim, D. Hansora, P. Sharma, J.-W. Jang, J. S. Lee, *Chem. Soc. Rev.* **2019**, *48*, 1908. c) H. Sun, X. Xu, H. Kim, W. Jung, W. Zhou, Z. Shao, *Energy Environ. Mater.* **2023**, *6*, e12441.

[14] a) A. Varma, A. S. Mukasyan, A. S. Rogachev, K. V. Manukyan, *Chem. Rev.* **2016**, *116*, 14493; b) A. Qayum, M. Guo, J. Wei, S. Dong, X. Jiao, D. Chen, T. Wang, *J. Mater. Chem. A* **2020**, *8*, 10989; c) A. Qayum, X. Peng, J. Yuan, Y. Qu, J. Zhou, Z. Huang, H. Xia, Z. Liu, D. Q. Tan, P. K. Chu, F. Lu, L. Hu, *ACS Appl. Mater. Interfaces* **2022**, *14*, 27842; d) H. Deng, A. Woldu, A. Qayum, Z. Huang, W. Zhu, X. Peng, P. Chu, L. Hu, *Chinese Chem. Lett.* **2024**, *35*, 109892.

[15] a) A. G. M. daSilva, T. S. Rodrigues, S. J. Haigh, P. H. C. Camargo, *Chem. Commun.* **2017**, *53*, 7135; b) C. M. Cobley, Y. Xia, *Mater. Sci. Eng. R: Rep.* **2010**, *70*, 44.

[16] D. Cao, D. Liu, S. Chen, O. A. Moses, X. Chen, W. Xu, C. Wu, L. Zheng, S. Chu, H. Jiang, C. Wang, B. Ge, X. Wu, J. Zhang, L. Song, *Energy Environ. Sci.* **2021**, *14*, 906.

[17] C. Jing, T. Yuan, L. Li, J. Li, Z. Qian, J. Zhou, Y. Wang, S. Xi, N. Zhang, H.-J. Lin, C.-T. Chen, Z. Hu, D.-W. Li, L. Zhang, J.-Q. Wang, *ACS Catal.* **2022**, *12*, 10276.

[18] a) E. Fabbri, M. Nachtegaal, T. Binninger, X. Cheng, B. J. Kim, J. Durst, F. Bozza, T. Graule, R. Schaublin, L. Wiles, M. Pertoso, N. Danilovic, K. E. Ayers, T. J. Schmidt, *Nat. Mater.* **2017**, *16*, 925; b) Y. Zhou, Y. Li, L. Zhang, L. Zhang, L. Li, J. Tian, M. Wang, J. Xu, B. Dai, Y. Li, *Chem. Eng. J.* **2020**, *394*, 124977.

[19] R.-Y. Fan, J.-Y. Xie, H.-J. Liu, H.-Y. Wang, M.-X. Li, N. Yu, R.-N. Luan, Y.-M. Chai, B. Dong, *Chem. Eng. J.* **2022**, *431*, 134040.

[20] F. Yang, Y. Luo, Q. Yu, Z. Zhang, S. Zhang, Z. Liu, W. Ren, H. M. Cheng, J. Li, B. Liu, *Adv. Funct. Mater.* **2021**, *31*, 2010367.

[21] X. Han, G. He, Y. He, J. Zhang, X. Zheng, L. Li, C. Zhong, W. Hu, Y. Deng, T. Y. Ma, *Adv. Energy Mater.* **2017**, *8*, 1702222.

[22] C. Alex, S. C. Sarma, S. C. Peter, N. S. John, *ACS Appl. Energy Mater.* **2020**, *3*, 5439.

[23] H. Hao, Y. Li, Y. Wu, Z. Wang, M. Yuan, J. Miao, Z. Lv, L. Xu, B. Wei, *Mater. Today Energy* **2022**, *23*, 100887.

[24] J. K. Nørskov, J. Rossmeisl, A. Logadottir, L. Lindqvist, J. R. Kitchin, T. Bligaard, H. Jónsson, *J. Phys. Chem. B* **2004**, *108*, 17886.

[25] J. Rossmeisl, Z. W. Qu, H. Zhu, G. J. Kroes, J. K. Nørskov, *J. Electroanal. Chem.* **2007**, *607*, 83.

NANO · MICRO
small

Supporting Information

for *Small*, DOI 10.1002/smll.202408854

Dynamically Reconstructed Fe-CoOOH Semi-Crystalline Electrocatalyst for Efficient Oxygen Evolution Reaction

Abdul Qayum, Karim Harrath, Rui Li, Abebe Reda Woldu, Paul K. Chu, Liangsheng Hu, Fushen Lu* and Xiangdong Yao*

Supporting Information

Dynamically reconstructed Fe-CoOOH Semi-Crystalline electrocatalyst for efficient oxygen evolution reaction

Abdul Qayum[a], Karim Harrath[b], Rui Li[a], Abebe Reda Woldu[a], Paul K.Chu[e], Liangsheng Hu[a,c,*], Fushen Lu[a,c,*] and Xiangdong Yao[c,d]

[a] Department of Chemistry and Key Laboratory for Preparation and Application of Ordered Structural Materials of Guangdong Province, Shantou University, Shantou, Guangdong, 515063, P. R. China

[b] Fundamental Science Center of Rare Earths, Ganjiang Innovation Academy, Chinese Academy of Science, Guanzhou 341000, P. R. China

[c] Chemistry and Chemical Engineering Guangdong Laboratory, Shantou, 515063, P. R. China

[d] School of Advanced Energy, Sun Yat-sen University (Shenzhen), Shenzhen 518107, P. R. China

[e] Department of Physics, Department of Materials Science and Engineering, and Department of Biomedical Engineering, City University of Hong Kong, Hong Kong, P. R. China

ORCID: 0000-0002-3323-7181(F.S. Lu); 0000-0002-4133-2090 (L.S. Hu)

*Correspondence: fslu@stu.edu.cn (F.S. Lu), lshu@stu.edu.cn (L.S. Hu)

Experimental Details

Materials

All the reagents and materials were used without further refinement. Ethylene glycol (EG), $Fe(NO_3)_3 \cdot 9H_2O$, and $Co(NO_3)_2 \cdot 6H_2O$, $Ni(NO_3)_2.9H_20$, $Cu(NO_3)_2.6H_2O$ were received from Shanghai Macklin Biochemical Co. Ltd., and Pt/C, KOH, and RuO_2 were bought from Aladdin Industrial Corporation. Co foam was obtained from TengErHui Co. Ltd.

Fabrication of Fe-CoOOH/CF

A rapid, single-step *in situ* solution combustion method was employed to synthesize the $CoFeO_x$/CF pre-catalyst. To carry out the combustion reaction, a precursor solution consisting of $Fe(NO_3)_3.9H_2O$ (oxidizer) and ethylene glycol (fuel, solvent) was prepared. Before the combustion process, the CF substrate ($0.5 \times 3 \times 0.15$ cm^3) was placed on a hot plate and heated to 180 °C. An optimized amount of precursor solution (100 μL cm^{-2}, 0.48M) was drop-casted onto the CF, and a rapid ($\leq$ 5 min.) combustion reaction was carried out to grow highly porous and small $CoFeO_x$ nanoparticles on the surface of the CF. During the combustion process, the outer surface of the CF reacted with a combustive solution and yielded $CoFeO_x$ nanoparticles.

The desirable transformation of the $CoFeO_x$ pre-catalyst to Fe-CoOOH/CF electrocatalyst was achieved quickly by the *in situ* electrochemical reconstruction process, which was carried out by both cyclic voltammetry (CV) and

chronopotentiometry (CP) under OER conditions. CV was carried out using the potential range of 1-1.6 V vs RHE at a scanning rate of 5 mV sec^{-2}, and the CP analysis was examined at a current density of 1,000 mA cm^{-2}. Two CV cycles are needed to reconstruct the surface and reach maximum current density, while a few minutes were required to attain surface rebuilding and maximum OER activity in the CP activation process. To elucidate the unique beneficial effect of Fe doping in the CoOOH structure, undoped CoOOH, Ni, and Cu-doped CoOOH catalysts were synthesized by the same synthesis method and reconstruction protocol as for Fe-CoOOH.

Characterization

Field-emission scanning electron microscopy (SEM, Gemini 300), and transmission electron microscopy (TEM, JEOL JEM-200) were used to examine the initial morphology and surface evaluation of the precatalyst and the reconstructed electrocatalysts. The chemical states were monitored by X-ray photoelectron spectroscopy (XPS, Thermo Fisher Scientific K-Alpha). The weight loss and heat dynamics during the combustion reaction were studied with the aid of the thermogravimetry-mass spectra (TG-DSC) obtained in air on the NETZSCH STA449F3-QMS403D. The *in situ* Raman analysis was conducted on a micro-Raman (LabRAM HR800) spectrometer, and the Fourier transform infrared (FTIR) spectra were acquired using KBr pellets (IR 200).

Electrochemical measurements

The electrochemical properties of the Fe-CoOOH/CF electrocatalyst and control were determined on a CHI760E potentiostat (CH Instruments Inc. China) with a three-electrode arrangement. The as-constructed Fe-CoOOH/CF electrocatalyst and control samples were the working electrodes, and a Pt-rod electrode was the counter electrode. The standard Hg/HgO electrode was the reference electrode and the electrolyte was 1 M KOH. For comparison, a mixture containing 1 mL ethanol-water (v/v = 1:1) consisting of 50 μL Nafion (5%, DuPont) was utilized to disperse the commercial RuO_2 powder to fabricate the RuO_2/CF electrocatalyst. (~ 6 mg cm^{-2}). The OER, overall water splitting, and electrochemical properties were recorded with the best practices using the partial immersion method and epoxy to control the active area of the sample during the electrochemical test. The OER and water splitting activities were examined by CV and LSV at a scanning rate of 5 mV sec^{-1}. C_{dl} was measured in a non-Faradic region (±50 mV of open circuit potential (OCP) by recording CV at various scan rates (1-5 mV sec^{-1}). Before the measurement, the OCP was stabilized by carrying out the CP for 5 min at 100 mA cm^{-2}. The long stability test (1,000 h) was performed in a partially controlled environment with temperature fluctuation within 18-25 °C during the test. The electrolyte was refreshed after each 100 h. Electrochemical impedance spectroscopy (EIS) was conducted with an amplitude of 5 mV at 1.55 V vs RHE in a frequency range of 100 kHz to 0.1 Hz. To determine the double-layer capacitance (C_{dl}), the CV curves were recorded at scanning rates of 1, 2, 3, 4, and 5 mV s^{-1} in the non-Faradaic potential window. The LSV, CV, chronopotentiometry, and multicurrent

curves in OER and water splitting were iR corrected. The potentials were obtained with the Hg/HgO reference electrode and later changed to the RHE according to the standard Nernst equation ($E_{(RHE)} = E_{(Hg/HgO)} + 0.098 + 0.059$ V × pH).

Density-functional theory calculations

The spin-polarized density functional theory (DFT) calculations with the Perdew-Burke-Ernzerhof (PBE) exchange-correlation functional[1] were performed using the Vienna ab initio simulation package (VASP).[2] The Hubbard correction of DFT+U was applied to Co and Fe atoms with a value of 3.5 eV.[3,4] The projector augmented wave method (PAW) [5,6] with a plane-wave kinetic energy cutoff of 400 eV was used, with the Gaussian smearing of 0.05 eV. The Brillouin zone was sampled by 3×3×1 K-point for geometry optimization, and 6×6×1 K-point to calculate the PDOS. The supporting CoOOH (100) surface was modeled by a (2 × 2) supercell and a vacuum layer of 15 Å. All the atoms were allowed to relax during geometry optimization, and the atomic positions were optimized until the forces were less than 0.03 eV/Å. The structure of the isolated molecules (O_2, H_2, and H_2O) was optimized within a unit cell measuring 15Å×15 Å×15 Å, with only the Γ-point utilized.[7] The effects of van der Waals corrections were modeled using Grimme's method with Becke–Jonson damping.[8,9]

The binding energy of metal atoms is defined as: $E_{binding}^{M} = E_{total} - E_{surafce} - EM$), where $E_{surafce}$, EM, and E_{total} are the energies of the CoOOH clean surface, M is the atom in the gas phase extracted from the bulk and metal adsorbed on the surface, respectively. The OER performance of pure and doped pentlandites

systems can be predicted using the Gibbs free-energy (ΔG) profiles for the following sequence of elementary OER sub-steps, according to Norskov et *al.*[10]:

Step I: $OH^- + * \rightarrow *OH + e^-$

Step II: $*OH + OH^- \rightarrow *O + H_2O + e^-$

Step III: $*O + OH^- \rightarrow *OOH + e^-$

Step IV: $*OOH \rightarrow * + O_2 + e^-$,

where * represents the bare site, and *OH, *O, $*O_2$, and *OOH denote the surface featuring different chemisorbed species. The free energy difference for all of the elementary steps above (ΔGOH*, ΔGO*, ΔGOOH*) involving electron transfer is calculated by the equation: $\Delta G = \Delta E + \Delta ZPE - T\Delta S + \Delta G\, U + \Delta G\, pH$, where ΔE, ΔZPE, and ΔS correspond to the energy difference between adsorption energy, zero-point energy, and entropy, respectively. The adsorption energies ΔE were derived by DFT, and ΔZPE and TΔS were obtained by the vibrational frequency calculations and DFT: ΔGU = −eU, where U represents a potential based on a standard hydrogen electrode, ΔGpH is the Gibbs free energy correction of the pH. A pH of 0 was used in the computation. The free energy profiles for OER calculated in this work using the standard hydrogen electrode (SHE) as a reference.

Under ideal conditions, the OER with a total energy change of 4.92 eV can be driven at 1.23 V, while the free energy of each elementary reaction is divided equally into 1.23 eV. Therefore, the overpotential η is introduced to represent the additional required potential and rationalize the catalytic performance of the catalyst, which is defined in theoretical calculations as $\eta = \max(\Delta G_{(1,2,3,4)})/e - 1.23$ eV.

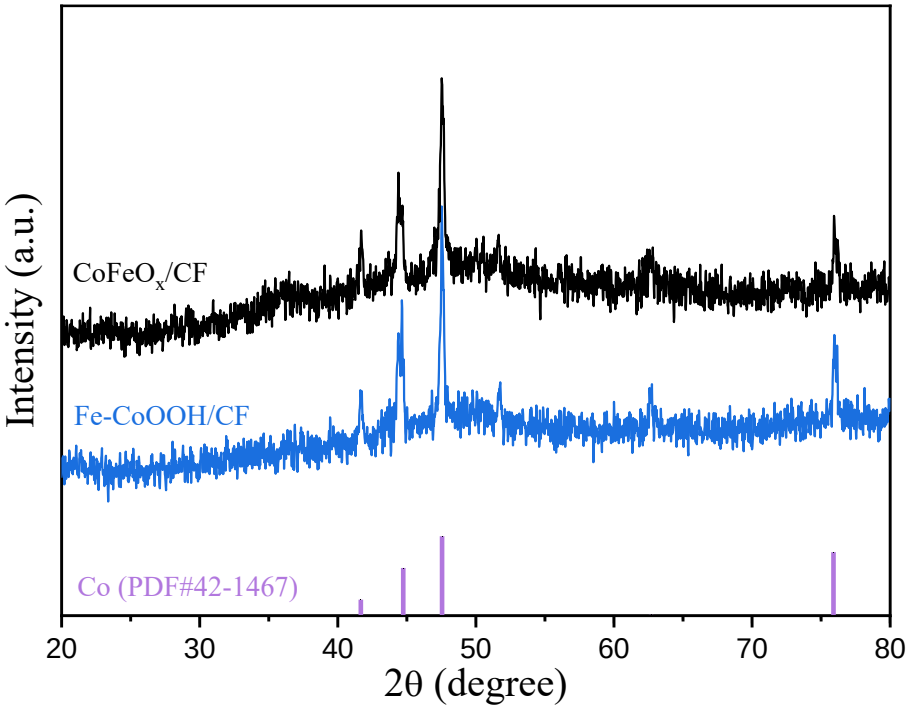

Figure S1. XRD pattern of the $CoFeO_x$ pre-catalyst and reconstructed Fe-CoOOH/CF electrocatalyst.

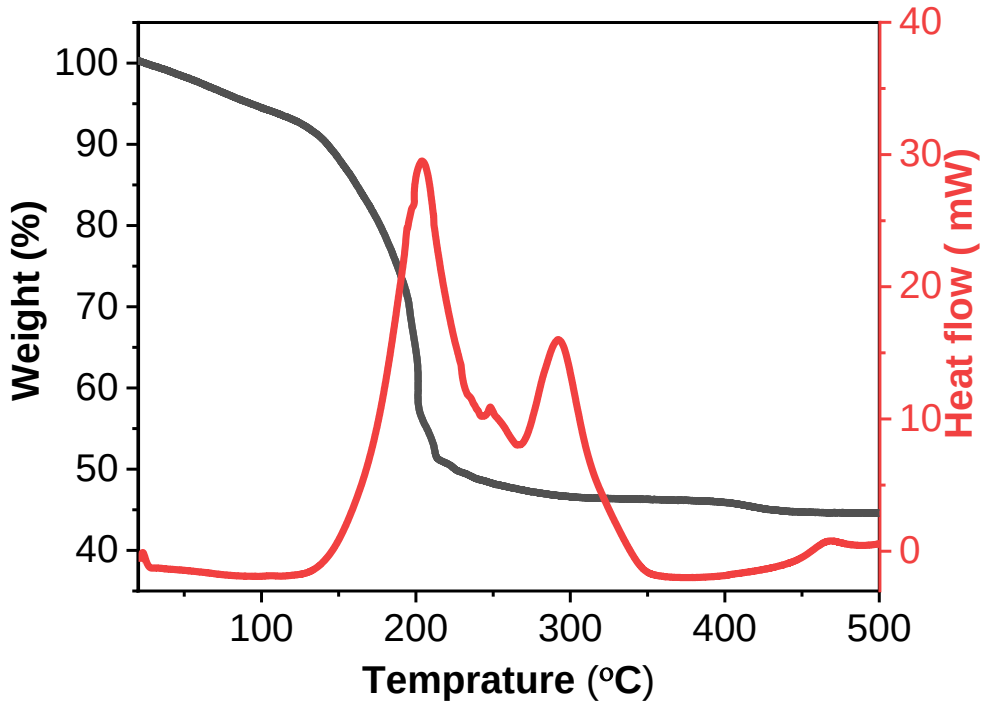

Figure S2. TGA and DSC curves of the precursor solution.

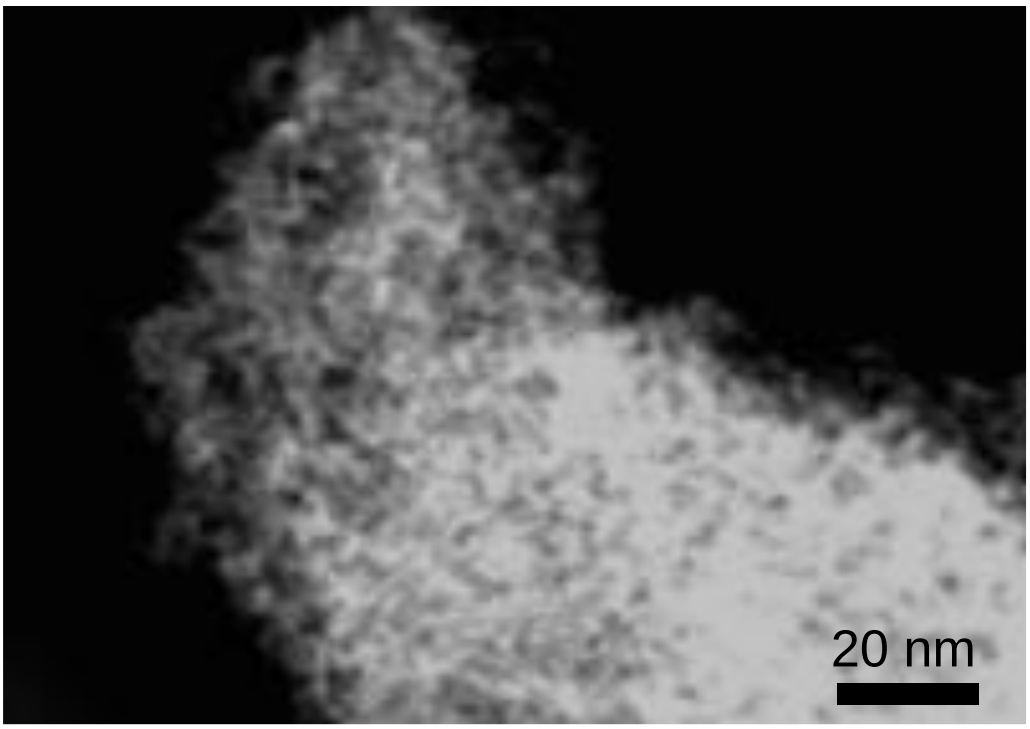

Figure S3. High-angle annular dark-field (HAADF) TEM image of the Fe-CoOOH/CF electrocatalyst.

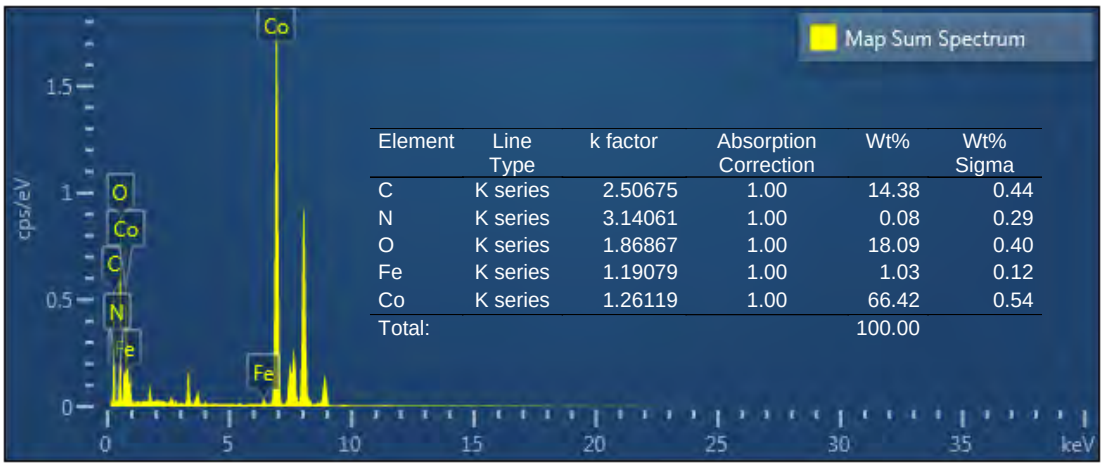

Element	Line Type	k factor	Absorption Correction	Wt%	Wt% Sigma
C	K series	2.50675	1.00	14.38	0.44
N	K series	3.14061	1.00	0.08	0.29
O	K series	1.86867	1.00	18.09	0.40
Fe	K series	1.19079	1.00	1.03	0.12
Co	K series	1.26119	1.00	66.42	0.54
Total:				100.00	

Figure S4. TEM-EDS elemental composition of the reconstructed Fe-CoOOH/CF electrocatalyst.

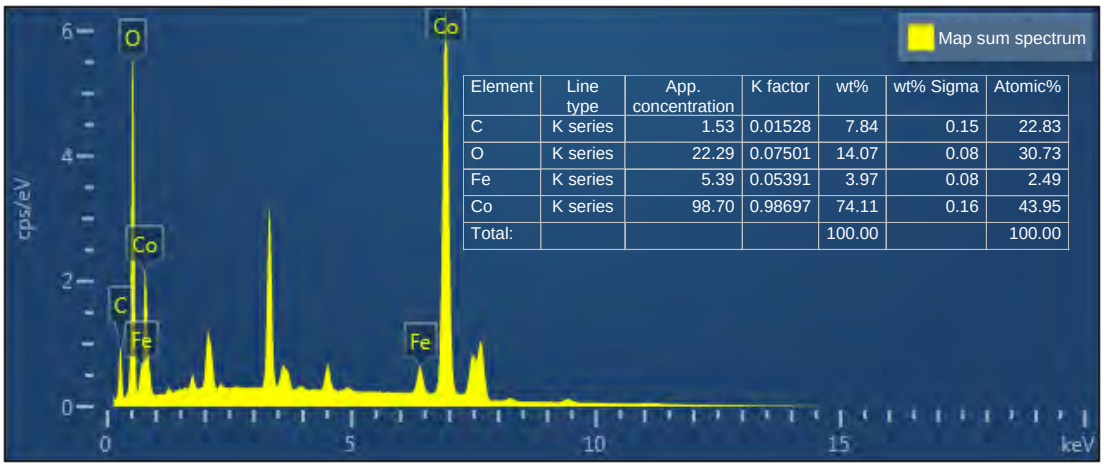

Element	Line type	App. concentration	K factor	wt%	wt% Sigma	Atomic%
C	K series	1.53	0.01528	7.84	0.15	22.83
O	K series	22.29	0.07501	14.07	0.08	30.73
Fe	K series	5.39	0.05391	3.97	0.08	2.49
Co	K series	98.70	0.98697	74.11	0.16	43.95
Total:				100.00		100.00

Figure S5. SEM-EDS elemental composition of the reconstructed Fe-CoOOH/CF electrocatalyst.

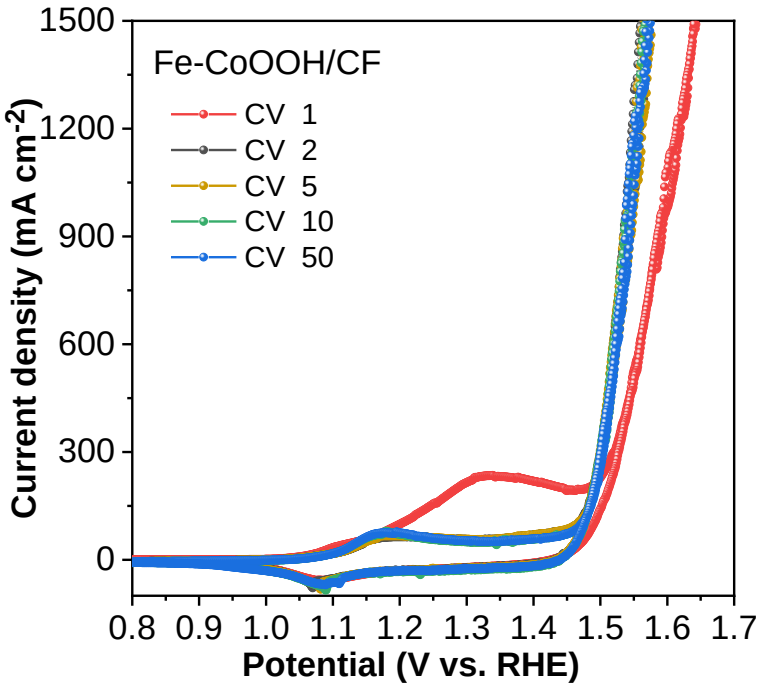

Figure S6. Cyclic Voltammetry curves of the Fe-CoOOH/CF electrocatalyst.

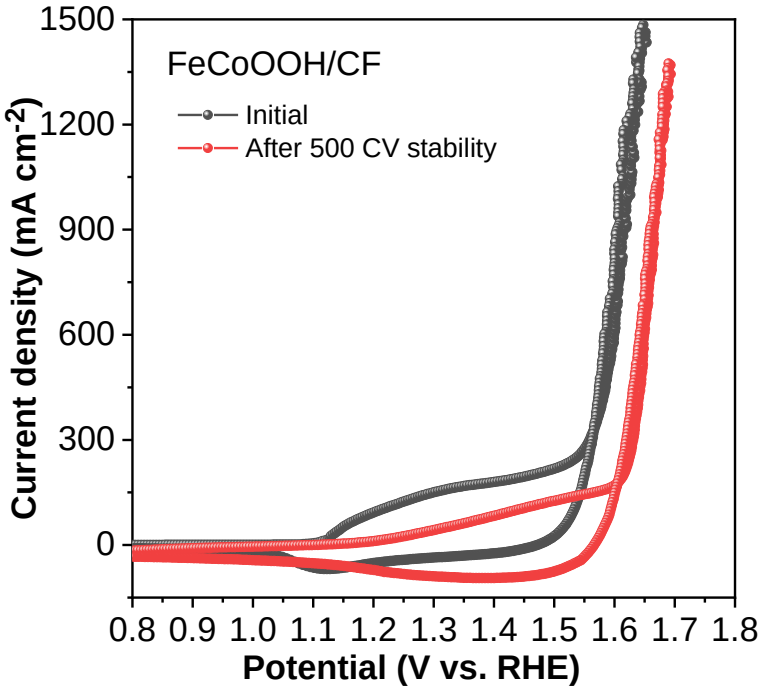

Figure S7. Cyclic Voltammetry curves of the Fe-CoOOH/CF electrocatalyst before and after 500 cycles.

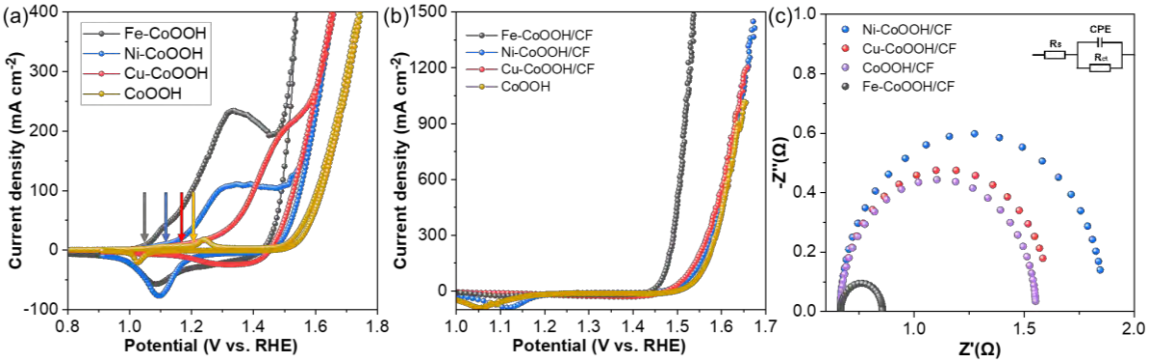

Figure S8. (a) Cyclic Voltammetry curves, (b) OER LSV curves, and (c) EIS data of the undoped and Fe, Ni, and Cu-doped CoOOH samples.

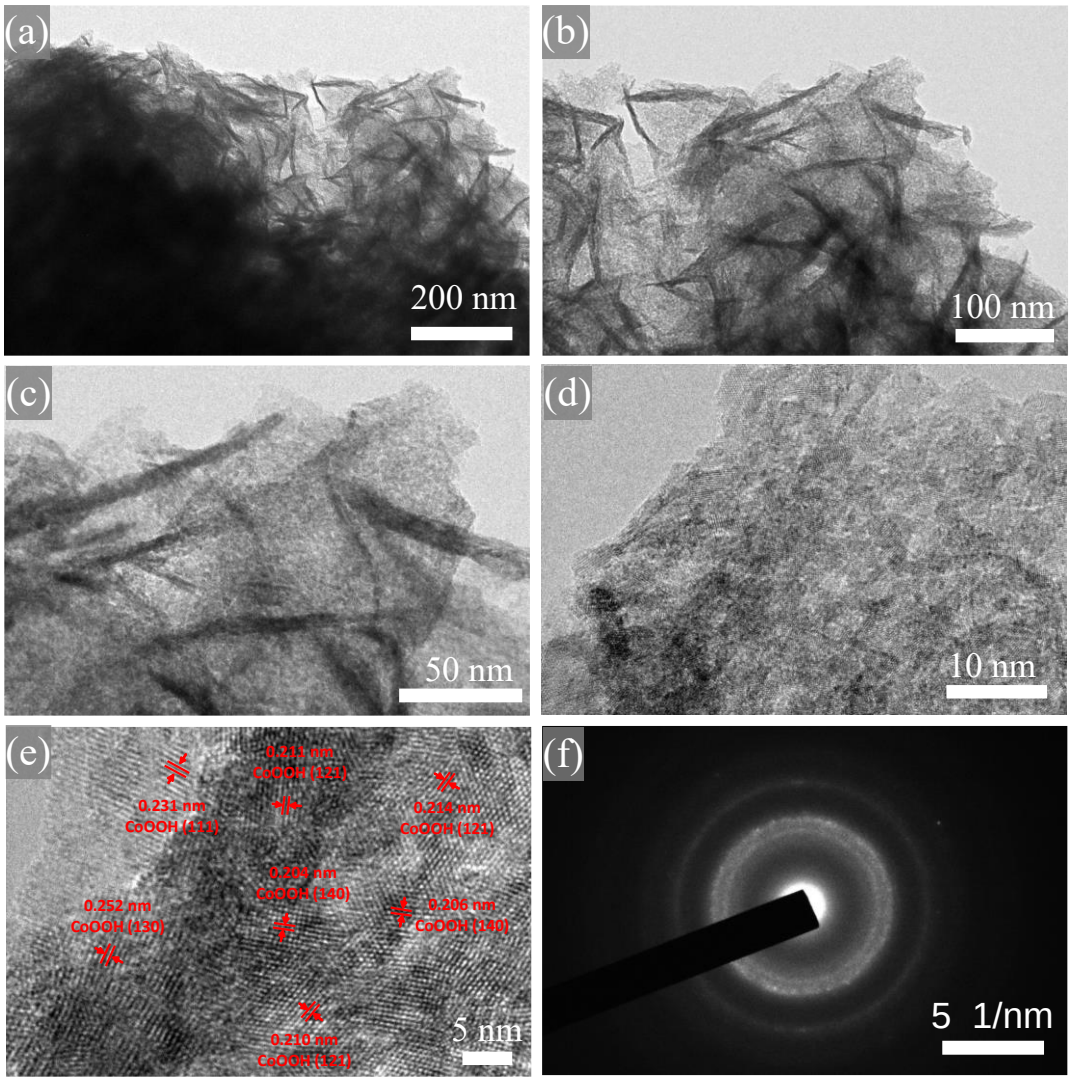

Figure S9.(a – d) TEM images, (e) HR-TEM image, and (f) SAED pattern of the CoOOH/CF electrocatalyst.

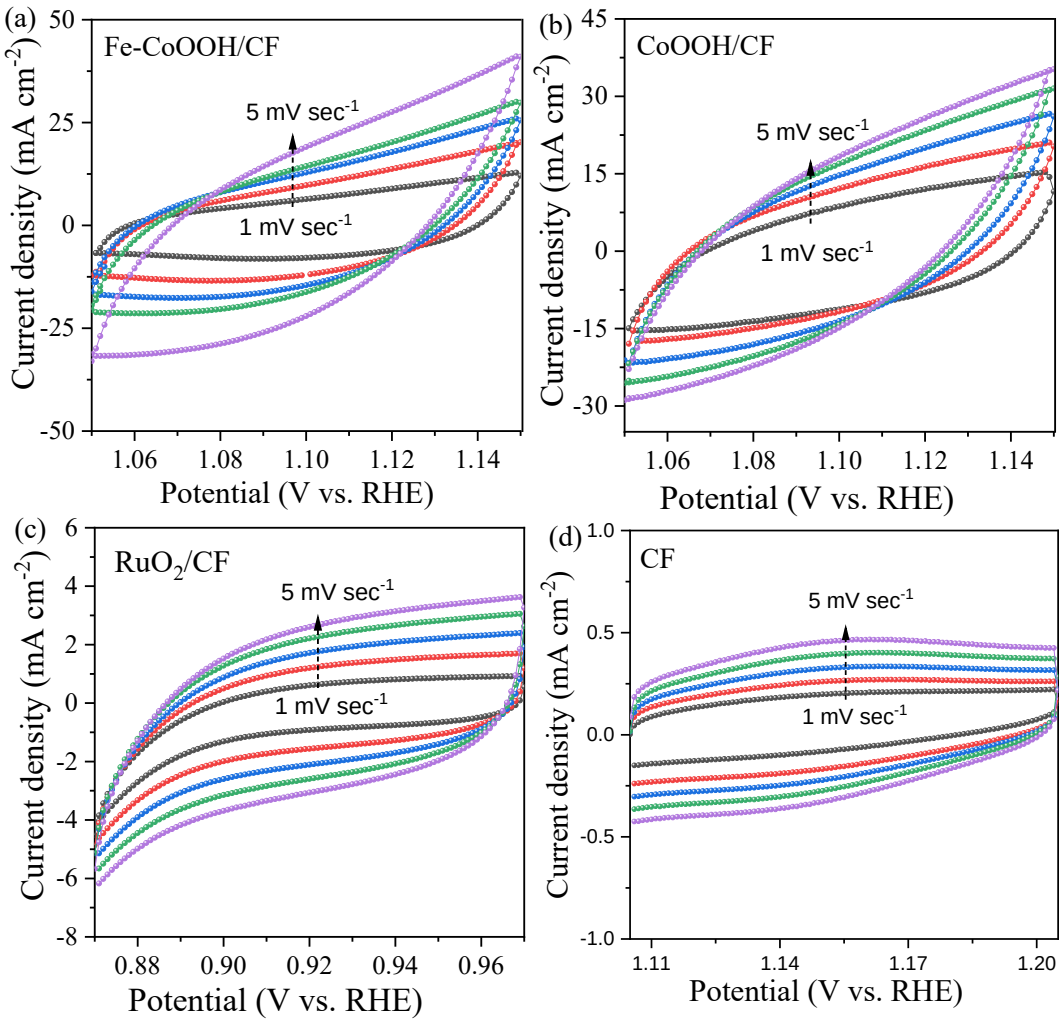

Figure S10. Raw CV data for the ECSA determination of the the (a) Fe-CoOOH/CF, (b) CoOOH/CF, (c) RuO2/CF and (d) CF.

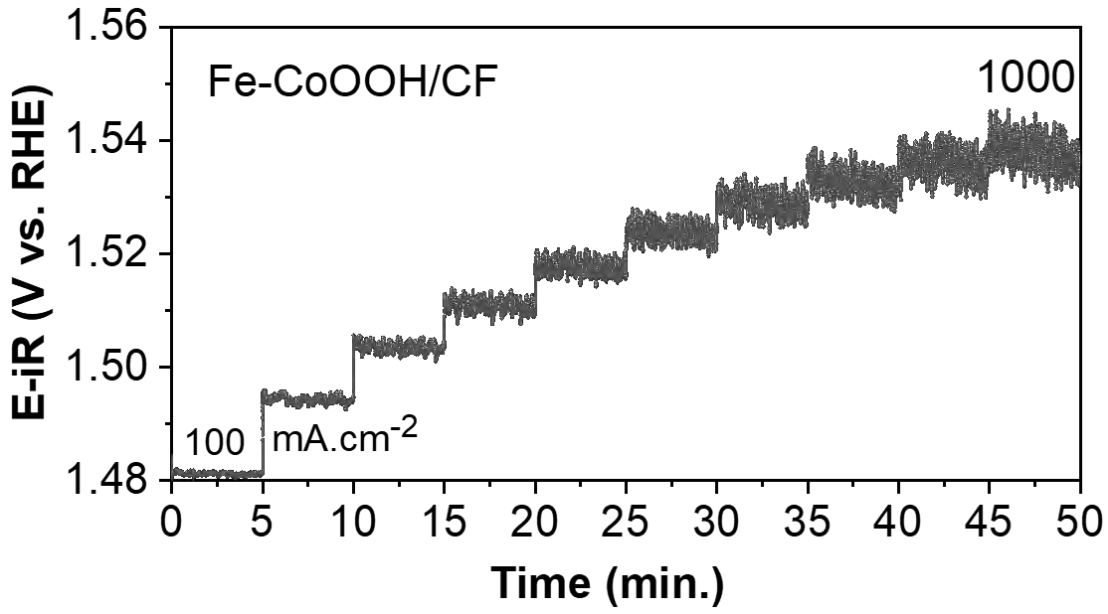

Figure S11. OER multicurrent chronopotentiometry curve of the Fe-CoOOH/CF electrocatalyst.

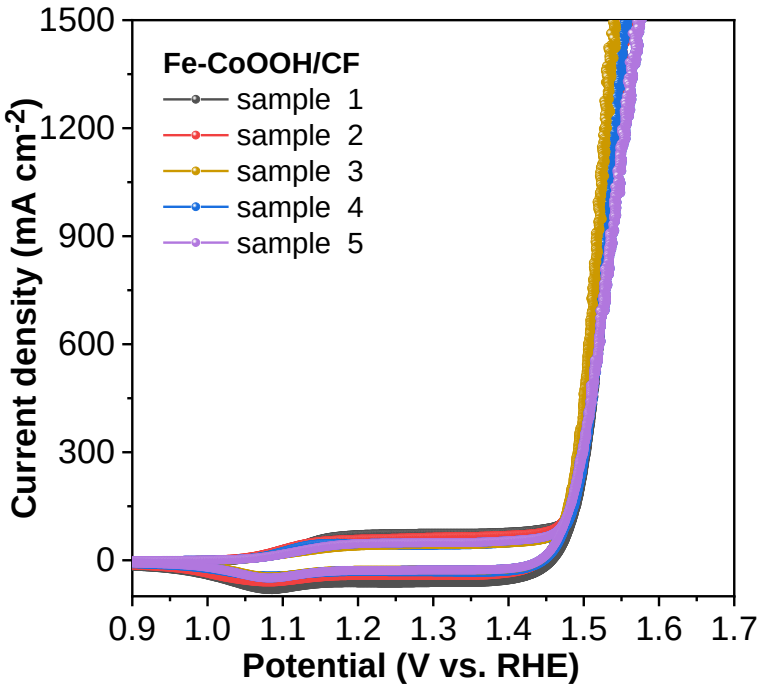

Figure S12. LSV OER curves of five different samples of Fe-CoOOH/CF, showing the excellent reproducibility of the *in situ* solution combustion method.

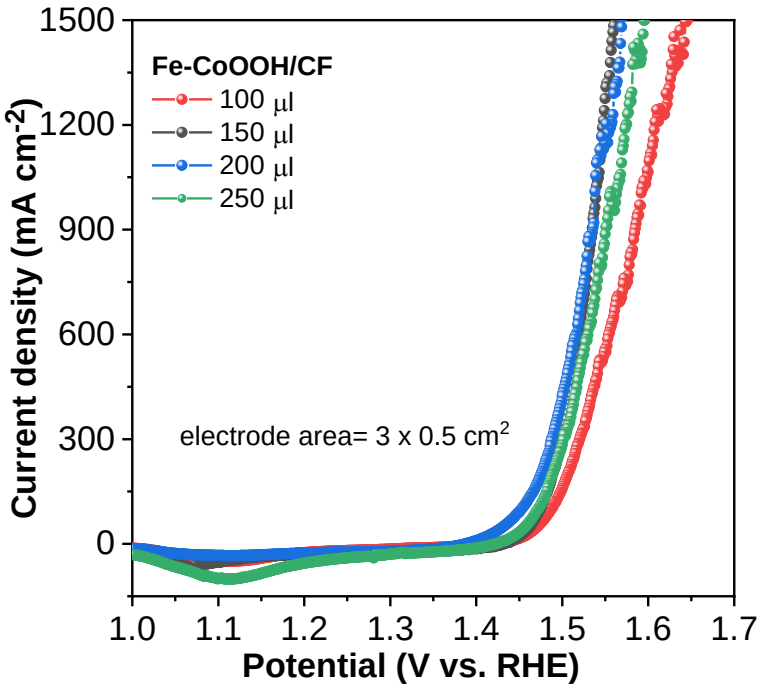

Figure S13. Effects of the amount of precursor solution deposited on CF (3 x 0.5 cm^2) on the OER activity of Fe-CoOOH/CF catalyst.

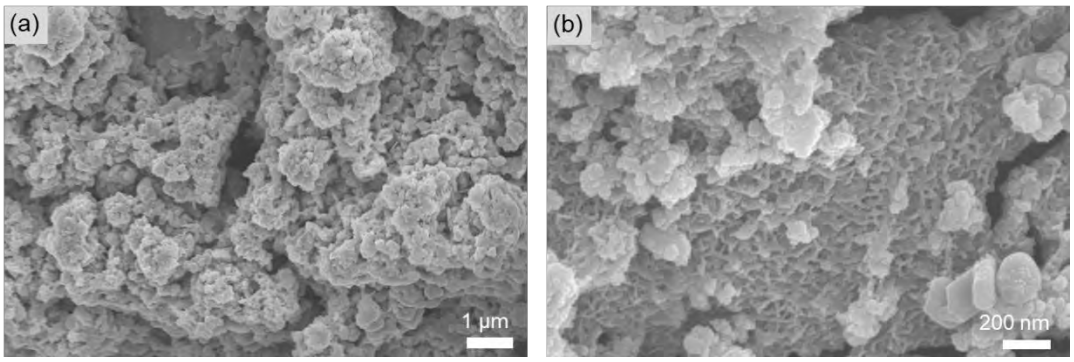

Figure S14. SEM images of the Fe-CoOOH/CF catalyst after long 100- h OER activity.

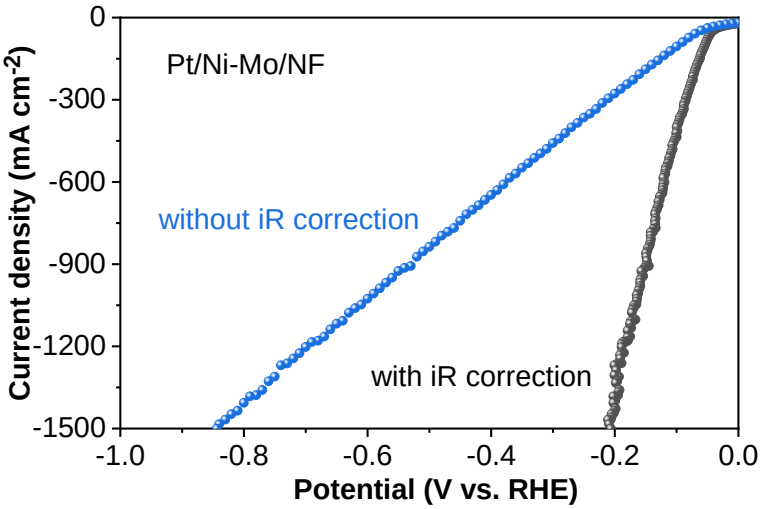

Figure S15. HER LSV curves of the Pt/Ni-Mo/NF catalyst with and without iR correction.

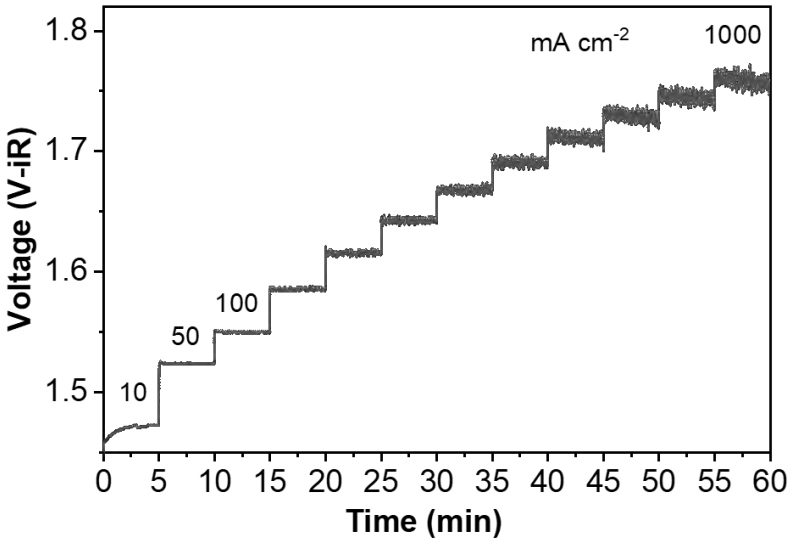

Figure S16. Overall water splitting multicurrent chronopotetiometric curve of the Fe-CoOOH/CF(+)//Pt/Ni-Mo/NF(-) electrolyzer pair.

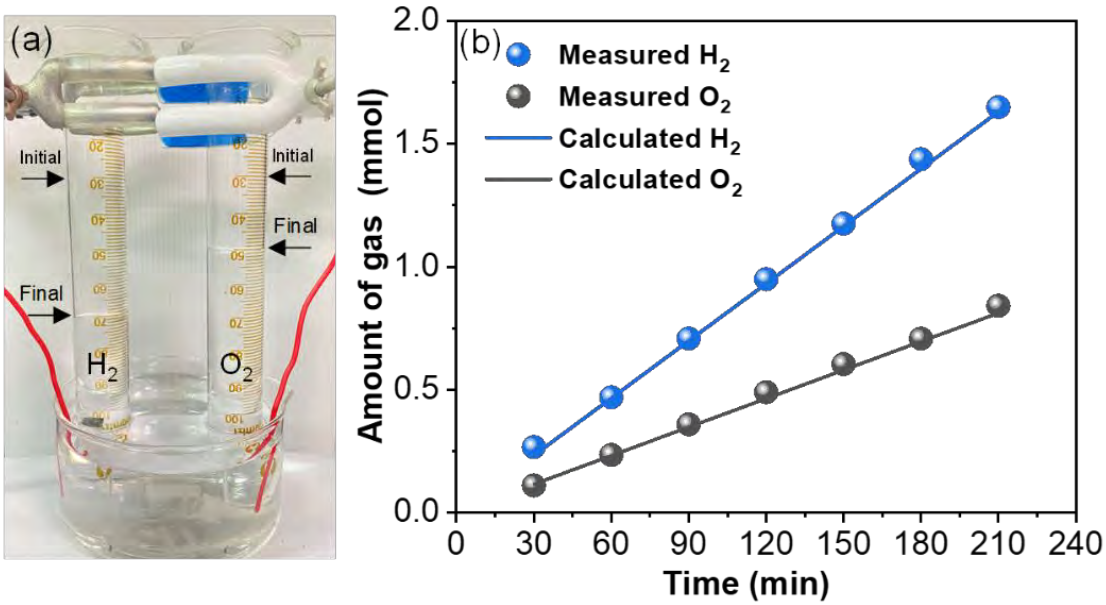

Figure S17. (a) Photograph of the two-electrode water splitting with the Fe-CoOOH/CF(+)//Pt/Ni-Mo/NF(-) electrolyzers and H_2/O_2 gas generation measured by the water displacement method; (b) Experimental and theoretical amounts of H_2/O_2 produced at a current density of 100 mA.cm^{-2}.

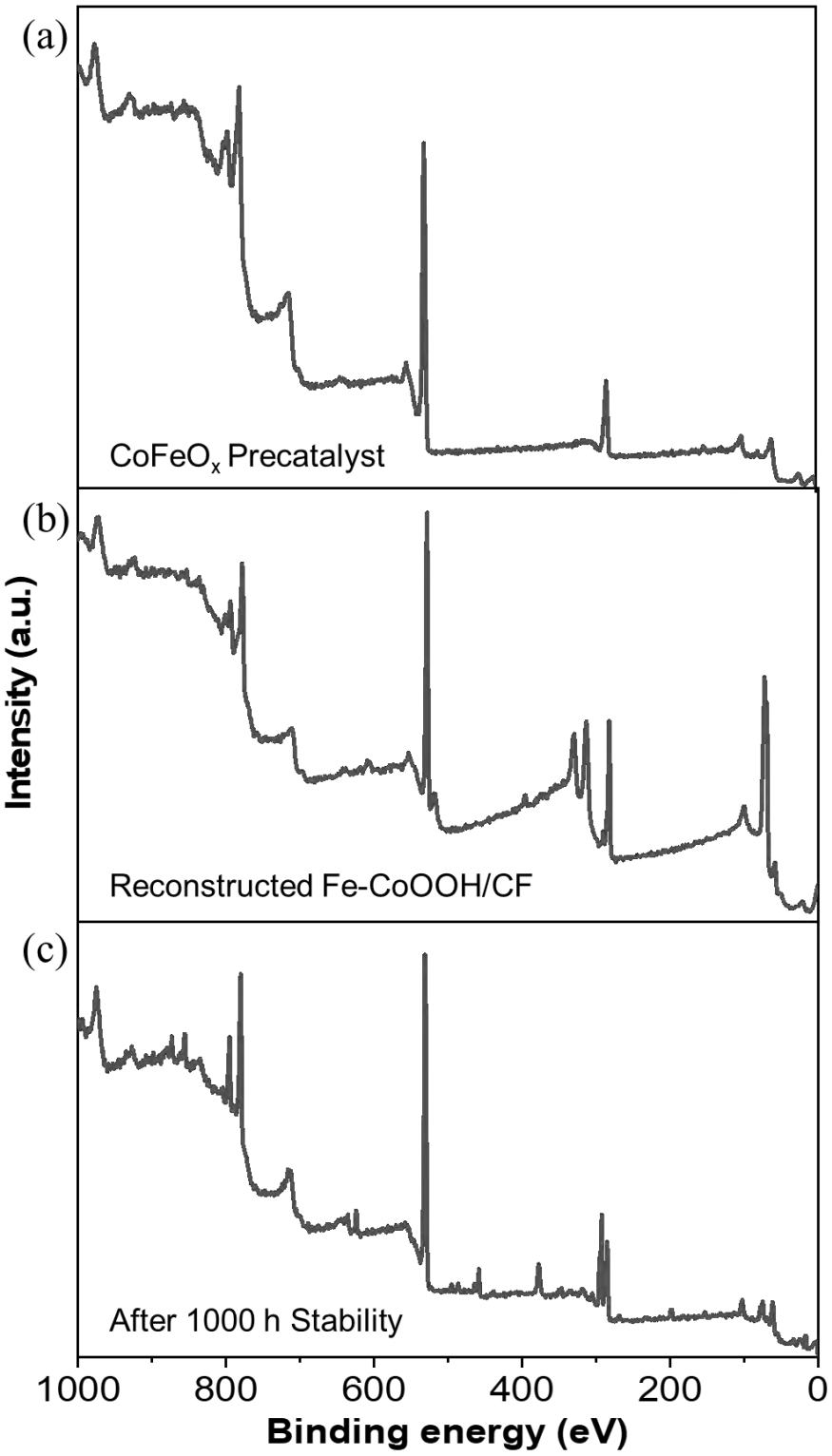

Figure S18. XPS survey spectra: (a) $CoFeO_x$/CF pre-catalyst, (b) Reconstructed Fe-CoOOH/CF sample, and (c) After long 1000-h OER stability.

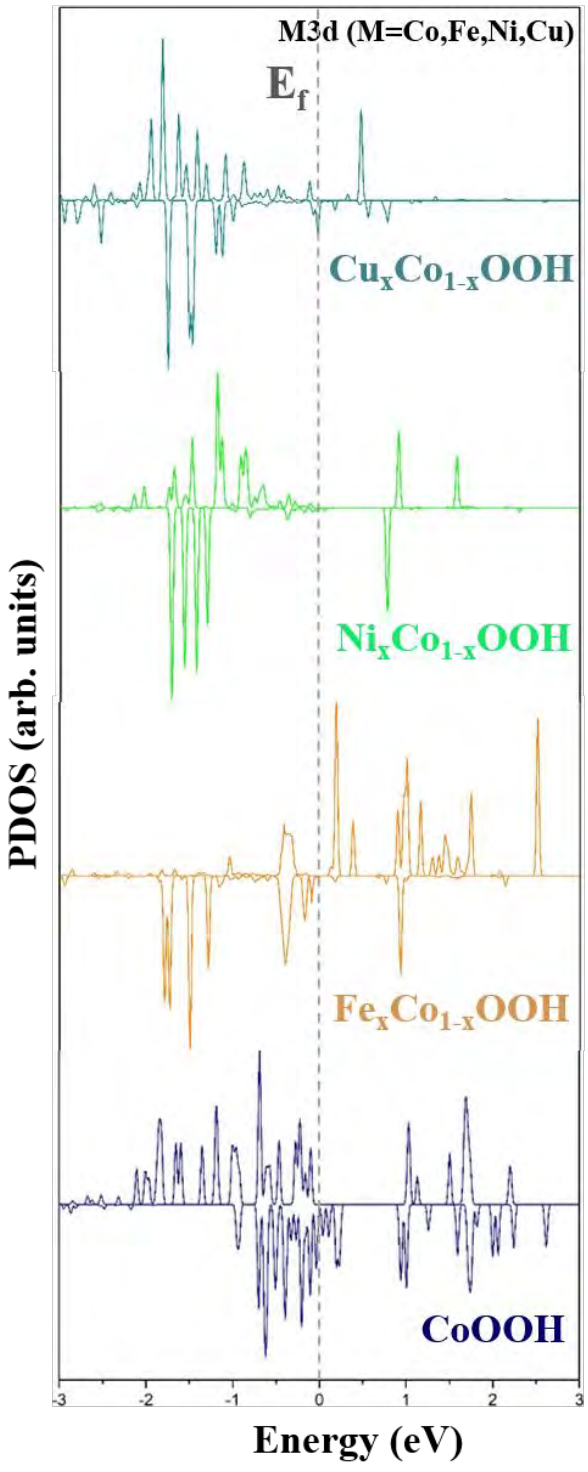

Figure S19. Co, Fe, Ni, and Cu 3*d* projected density of states (PDOS) in CoOOH, $Fe_xCo_{1-x}OOH$, $Ni_xCo_{1-x}OOH$, and $Cu_xCo_{1-x}OOH$.

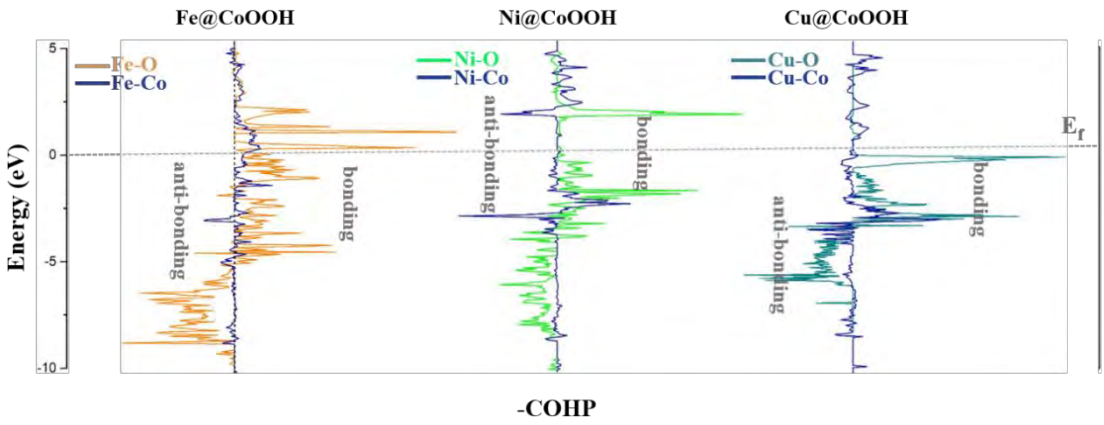

Figure S20. COHP of Fe-CoOOH, Ni-CoOOH, and Cu-CoOOH.

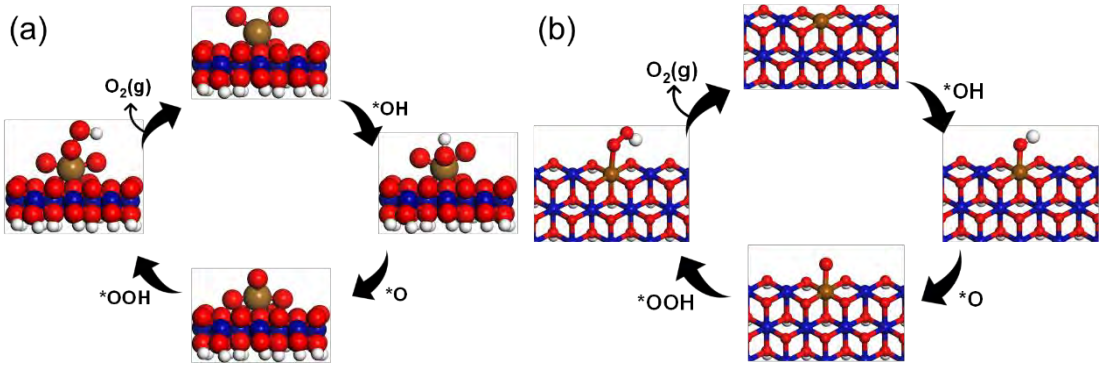

Figure S21. (a) Schematic showing the OER pathway on FeO_2-CoOOH and (b) Schematic of the OER pathway on $Fe_xCo_{1-x}OOH$.

Table S1. Comparison of the OER properties of Fe-CoOOH/CF catalyst with those of recently reported state-of-the-art electrocatalysts synthesized on foamy substrates with $j_{HCD} \geq 1000$ mA cm^{-2}.

Catalysts	**Synthetic methods**	**Overpotentials (mV)@1A cm^{-2}**	**Tafel Slopes (mV dec^{-1})**	**Stability (h)**	**Refs.**
$BiCoO_3$	Solid-state reaction	402	44	110	13
NiMoN/NiFe LDH	Hydrothermal + Nitridation	266	42.2	250	14
NiFeOOH	Electrodeposition	315	54.4	100	15
CoFe LDH	Stirring + Solvothermal	310	38	150	16
Ru-Ni(Fe)P_2/NF	Hydrothermal + CVD	375	91.6	50	17
$Mn_{0.15}$-NiFe LDH/$Fe_{0.64}Ni_{0.36}$	Electrodeposition + Etching	340	16.3	250	18
Cr-FeOOH/$FeSe_2$	Electrodeposition	374	54.5	80	19
R-NiFeO_xH	Hydrothermal	313	44.7	500	20
SR-NiFeMoO	Hydrothermal	384	55.1	110	21
KT-Ni(0)@Ni(II)-TPA	Hydrothermal	380	-	50	22
Ni_3N@2M-MoS_2	Hydrothermal + CVD	327	38.9	300	23
S-FeOOH	Electrochemical active	528	50.8	1000	24
Zn-(Ni/FeOOH)	Electrodeposition	330@	33	1000	25
Ni/Fe_3O_4/IF	Hydrothermal	338	44	100	26
$NiCoS_xSe_y$	Hydrothermal	390	42	100	27
BM/$BiFeO_xH_y$	Solvothermal	370	34	1000	28
MnO_x/NiFeP	Hydrothermal + Electrodeposition	346	59.8	120	29
$FeNiCoCrMnS_2$	Solvothermal	308	39.1	55	30
Fe-CoOOH	*In situ* combustion + electrochemical	291 307	35.6	1000	This work

Notes: NSPs, nanospheres; NSs, Nanosheets; NFs, Nanoflakes, CVD; Chemical vapor deposition.

References

1. Man, I. C.; Su, H. Y.; Calle-Vallejo, F.; Hansen, H. A.; Martínez, J. I.; Inoglu, N. G.; Kitchin, J.; Jaramillo, T. F.; Nørskov, J. K.; Rossmeisl, J. J. C., Universality in oxygen evolution electrocatalysis on oxide surfaces. ChemCatChem 2011**,** *3* (7), 1159-1165. 2011, 3 (7), 1159-1165.

2. http://www.vasp.at; version vasp.5.3.5

3. Tang, M.; Ge, Q. J. C. J. o. C., Mechanistic understanding on oxygen evolution reaction on γ-FeOOH (010) under alkaline condition based on DFT computational study. Chinese Journal of Catalysis 2017, 38 (9), 1621-1628.

4. Bajdich, M.; García-Mota, M.; Vojvodic, A.; Nørskov, J. K.; Bell, A. T. J. J. o. t. A. c. S., Theoretical investigation of the activity of cobalt oxides for the electrochemical oxidation of water. Journal of the American Chemical Society 2013, 135 (36), 13521-13530.

5. Kresse, G.; Joubert, D. J. P. r. b., From ultrasoft pseudopotentials to the projector augmented-wave method. Physical review B 1999, 59 (3), 1758.

6. Blöchl, P. E. J. P. r. B., Projector augmented-wave method. Physical review B 1994, 50 (24), 17953.

7. Bahri, L.; Mbarki, F.; Harrath, K. J. C. P., Understanding the direct methane conversion to oxygenates on graphene-supported single 3d metal atom catalysts. Chemical Papers 2023, 1-9.

8. Grimme, S.; Antony, J.; Ehrlich, S.; Krieg, H. J. T. J. o. c. p., A consistent and accurate ab initio parametrization of density functional dispersion correction (DFT-D)

for the 94 elements H-Pu. The Journal of chemical physics 2010, 132 (15).

9. Grimme, S. J. W. I. R. C. M. S., Density functional theory with London dispersion corrections. Wiley Interdisciplinary Reviews: Computational Molecular Science 2011, 1 (2), 211-228.

10. Nørskov, J. K.; Rossmeisl, J.; Logadottir, A.; Lindqvist, L.; Kitchin, J. R.; Bligaard, T.; Jonsson, H. Origin of the overpotential for oxygen reduction at a fuel-cell cathode. The Journal of Physical Chemistry B 2004, *108* (46), 17886-17892.

11. Rossmeisl, J.; Qu, Z.-W.; Zhu, H.; Kroes, G.-J.; Nørskov, J. K. Electrolysis of water on oxide surfaces. Journal of Electroanalytical Chemistry 2007**,** *607* (1-2), 83-89.

12. Hu, Y.; Li, L.; Zhao, J.; Huang, Y.-C.; Kuo, C.-y.; Zhou, J.; Fan, Y.; Lin, H.-J.; Dong, C.-L.; Pao, C.-W. Large current density for oxygen evolution from pyramidally-coordinated Co oxide. Applied Catalysis B: Environment and Energy 2023, *333*, 122785.

13. Zhai, P.; Wang, C.; Zhao, Y.; Zhang, Y.; Gao, J.; Sun, L.; Hou, J. Regulating electronic states of nitride/hydroxide to accelerate kinetics for oxygen evolution at large current density. Nature Communications 2023, *14* (1), 1873.

14. Zhang, Y.; Dastafkan, K.; Zhao, Q.; Li, J.; Zhao, C.; Liu, G. Stable tetravalent Ni species generated by reconstruction of FeB-wrapped NiMoO pre-catalysts enable efficient water oxidation at large current densities. Applied Catalysis B: Environmental 2024, *341*, 123297.

15. Li, D.; Xiang, R.; Yu, F.; Zeng, J.; Zhang, Y.; Zhou, W.; Liao, L.; Zhang, Y.; Tang, D.; Zhou, H. In Situ Regulating Cobalt/Iron Oxide-Oxyhydroxide Exchange by Dynamic Iron Incorporation for Robust Oxygen Evolution at Large Current Density. Advanced Materials 2024, *36* (5), 2305685.

16. Wu, D.; Liu, B.; Li, R.; Chen, D.; Zeng, W.; Zhao, H.; Yao, Y.; Qin, R.; Yu, J.; Chen, L. Fe-Regulated Amorphous-Crystal Ni(Fe)P_2 Nanosheets Coupled with Ru Powerfully Drive Seawater Splitting at Large Current Density. Small 2023, *19* (36), 2300030.

17. Qian, Y.; Zhang, F.; Qiu, L.; Han, W.; Zeng, Z.; Lei, L.; He, Y.; Li, P.; Zhang, X. Optimizing electronic structure of NiFe LDH with Mn-doping and $Fe_{0.64}Ni_{0.36}$ alloy for alkaline water oxidation under industrial current density. Nano Research 2023, *16* (7), 8953-8960.

18. Wang, J.; Xiang, Y.; Zhang, W.; Zhang, Y.; Zhao, Q.; Li, J.; Liu, G. Integrating Cr doped FeOOH into $FeSe_2$ nanoparticles for efficient water oxidation at large current densities. Fuel 2023, *351*, 128827.

19. Liu, J.; Du, W.; Guo, S.; Pan, J.; Hu, J.; Xu, X. Iron-locked hydr (oxy) oxide catalysts via ion-compensatory reconstruction boost large-current-density water oxidation. Advanced Science 2023, *10* (16), 2300717.

20. Zhang, Y.; Yao, R.; Wu, Y.; Zhao, Q.; Li, J.; Liu, G. In situ rapid and deep self-reconstruction of Fe-doped hydrate $NiMoO_4$ for stable water oxidation at high current densities. Chemical Engineering Journal 2023, *461*, 142081.

21. Hu, Q.; Wang, Z.; Huang, X.; Qin, Y.; Yang, H.; Ren, X.; Zhang, Q.; Liu, J.; Shao, M.; He, C. Integrating well-controlled core-shell structures into "superaerophobic" electrodes for water oxidation at large current densities. Applied Catalysis B: Environmental 2021, *286*, 119920.

22. Wu, T.; Song, E.; Zhang, S.; Luo, M.; Zhao, C.; Zhao, W.; Liu, J.; Huang, F. Engineering metallic heterostructure based on Ni_3N and 2M-MoS_2 for alkaline water electrolysis with industry-compatible current density and stability. Advanced Materials 2022, *34* (9), 2108505.

23. Zhang, X.-Y.; Li, F.-T.; Dong, Y.-W.; Dong, B.; Dai, F.-N.; Liu, C.-G.; Chai, Y.-M. Dynamic anion regulation to construct S-doped FeOOH realizing 1000 mA cm^{-2}-level-current-density oxygen evolution over 1000 h. Applied Catalysis B: Environmental 2022, *315*, 121571.

24. Zhang, X.; Yi, H.; Jin, M.; Lian, Q.; Huang, Y.; Ai, Z.; Huang, R.; Zuo, Z.; Tang, C.; Amini, A. In situ reconstructed Zn doped $Fe_xNi_{(1-x)}OOH$ catalyst for efficient and ultrastable oxygen evolution reaction at high current densities. Small 2022, *18* (37), 2203710.

25. Xu, W.; Zhong, W.; Yang, C.; Zhao, R.; Wu, J.; Li, X.; Yang, N. Tailoring interfacial electron redistribution of Ni/Fe_3O_4 electrocatalysts for superior overall water splitting. Journal of Energy Chemistry 2022, *73*, 330-338.

26. Ma, S.; Huang, J.; Zhang, C.; Chen, G.; Chen, W.; Shao, T.; Li, T.; Zhang, X.; Gong, T.; Ostrikov, K. K. One-step in-situ sprouting high-performance

$NiCoS_xSe_y$ bifunctional catalysts for water electrolysis at low cell voltages and high current densities. Chemical Engineering Journal 2022, *435*, 134859.

27. Jo, S.; Park, W. B.; Lee, K. B.; Choi, H.; Lee, K.-S.; Ahn, D.; Lee, Y.-W.; Sohn, K.-S.; Hong, J.; Sohn, J. I. Bi/BiFe (oxy) hydroxide for sustainable lattice oxygen-boosted electrocatalysis at a practical high current density. Applied Catalysis B: Environmental 2022, *317*, 121685.

28. Wang, P.; Luo, Y.; Zhang, G.; Wu, M.; Chen, Z.; Sun, S.; Shi, Z. MnO_x-decorated nickel-iron phosphides Nanosheets: Interface modifications for robust overall water splitting at ultra-high current densities. Small 2022, *18* (7), 2105803.

29. Nguyen, T. X.; Su, Y. H.; Lin, C. C.; Ting, J. M. Self-reconstruction of sulfate-containing high entropy sulfide for exceptionally high-performance oxygen evolution reaction electrocatalyst. Advanced Functional Materials 2021, *31* (48), 2106229.